Published in final edited form as:

Soft Matter. 2019 June 19; 15(24): 4873–4889. doi:10.1039/c9sm00536f.

Mechanisms of spontaneous chain formation and subsequent microstructural evolution in shear-driven strongly confined drop monolayers†

Sagnik Singha[a], **Abhilash Reddy Malipeddi**[b], **Mauricio Zurita-Gotor**[c], **Kausik Sarkar**[b], **Kevin Shen**[‡,d], **Michael Loewenberg**[d], **Kalman B. Migler**[e], **Jerzy Blawzdziewicz**[a,f]

[a]Department of Mechanical Engineering, Texas Tech University, Box 41021, Lubbock, TX 79409, USA.

[b]Department of Mechanical and Aerospace Engineering, George Washington University, Washington, DC 20052, USA

[c]Universidad Loyola Andalucia, Departamento de Ingeniería, Calle Energía Solar 1, 41014 Seville, Spain

[d]Department of Chemical and Environmental Engineering, Yale University, New Haven, USA

[e]Materials Science and Engineering Division, National Institute of Standards and Technology, Gaithersburg, Maryland 2089, USA

[f]Department of Physics and Astronomy, Texas Tech University, Box 41051, Lubbock, TX 79409, USA

Abstract

It was experimentally demonstrated by Migler and his collaborators [*Phys. Rev. Lett.*, 2001, **86**, 1023; *Langmuir*, 2003, **19**, 8667] that a strongly confined drop monolayer sheared between two parallel plates can spontaneously develop a flow-oriented drop-chain morphology. Here we show that the formation of the chain-like microstructure is driven by far-field Hele-Shaw quadrupolar interactions between drops, and that drop spacing within chains is controlled by the effective drop repulsion associated with the existence of confinement-induced reversing streamlines, *i.e.*, the swapping trajectory effect. Using direct numerical simulations and an accurate quasi-2D model that incorporates quadrupolar and swapping-trajectory contributions, we analyze microstructural evolution in a monodisperse drop monolayer. Consistent with experimental observations, we find that drop spacing within individual chains is usually uniform. Further analysis shows that at low area fractions all chains have the same spacing, but at higher area fractions there is a large spacing variation from chain to chain. These findings are explained in terms of uncompressed and compressed chains. At low area fractions most chains are uncompressed (spacing equals l_{st}, which is the stable separation of an isolated pair). At higher area fractions compressed chains (with

†Electronic supplementary information (ESI) available. See DOI: 10.1039/c9sm00536f

jerzy.blawzdziewicz@ttu.edu.

‡Present address: Materials Research Laboratory, MC 5121, University of California, Santa Barbara, CA 93106-5121, USA.

Conflicts of interest

There are no conflicts to declare.

tighter spacing) are formed in a process of chain zipping along y-shaped structural defects. We also discuss the relevance of our findings to other shear-driven systems, such as suspensions of spheres in non-Newtonian fluids.

1 Introduction

Flow-assisted formation of ordered structures in systems of rigid,[1–4] deformable,[5–13] and active,[14–20] particles has numerous important practical applications. Examples include particle control in microfluidic sorting devices[1,2,21–23] and manufacturing advanced microstructured materials (*e.g.*, microlens arrays,[24] nanostructured protein microfibers,[25] and filled polymeric materials with anisotropic properties[26–31]). Moreover, hydrodynamically induced interparticle coordination plays a significant role in pattern formation in biological matter.[32,33] Thus, spontaneous generation of patterns in non-equilibrium systems has practical and fundamental relevance.

Confinement gives rise to qualitatively new hydrodynamically driven collective dynamics. Confinement-induced collective phenomena include the formation of a variety of string-like microstructures in particulate systems in the creeping flow regime[13,34–37] and in microfluidic flows with inertia.[2] Hydrodynamic crystals (in 1D and 2D), which are stabilized by confinement,[21,38–43] exhibit complex dynamics, including wave propagation,[40] dislocations in a hydrodynamically ordered lattice,[42] fingering instabilities,[42] and buckling instabilities.[37]

Additional complexity of microstructural evolution arises from particle deformability. Ordered systems of confined hard spheres can be stabilized by flow. However, in the absence of such factors as inertia,[2] strong excluded-volume effects at high concentrations,[3] and/or nonlinearities associated with non-Newtonian properties of the suspending fluid, hard spheres do not spontaneously form ordered structures. By contrast, confined suspensions of deformable particles spontaneously self-assemble into a variety of structures under flow, [5,7,9,13,34,44–51] even at moderate volume fractions of the dispersed phase, *i.e.*, in the regime where the system evolution is dominated by hydrodynamic interactions rather than excluded-volume effects.[5,13,34,45–47,52–55]

To advance our understanding of confinement-induced spontaneous ordering of deformable particles, we investigate development of self-organized particle arrangements in systems of deformable drops in strongly confined shear flow in a narrow-gap Couette device. [5,45,47,52–54] Several years ago we suggested[10,56] that the observed spontaneous ordering of a drop monolayer into string-like arrangements oriented in the flow direction (pearlnecklace chain structures[45]) results from stabilization of flow-aligned drop arrays by the far-field Hele-Shaw quadrupolar interactions. Such hydrodynamic interactions between particles in narrow-gap parallel-wall channels are associated with the fluid flow driven by a quasi-2D far-field perturbation pressure with the four-fold quadrupolar symmetry.

In the present paper we expand on this premise, and explicitly show that key structural features of the system evolution can be faithfully described by a combination of the quadrupolar interactions and a hydrodynamic drop repulsion that results from the swapping

trajectory effect[57] in concert with the self-centering mechanism for confined deformable particles.[13,58]

At the core of our analysis is a simple quasi-2D model that combines the quadrupolar and swapping-trajectory contributions. The model correctly predicts microstructural evolution of a drop monolayer, as evidenced by a comparison with direct finite-difference front-tracking (FD/FT) simulations. We use this model to describe salient features of the drop-chain microstructure, including mechanisms of relaxation of microstructural defects and the evolution of drop spacing. The model allows us to efficiently investigate statistical aspects of the evolving monolayer morphology at long times, in the regime where direct simulations are not feasible due to a high numerical cost.

2 Summary of experimental observations

As illustrated in Fig. 1 (experimental images reprinted from ref. 5), a monolayer of drops undergoing shear flow between two parallel walls can spontaneously organize into "pearl-necklace" chains aligned with the flow. The drops in a chain may subsequently coalesce, which results in formation of elongated strings and ribbons. Our focus is on the system evolution before the coalescence into strings occurs, *i.e.*, on the process of formation of ordered drop arrangements and on the morphology of the spatial drop distribution.

Examples of self-organized ordered chains for different emulsion compositions, flow strengths, and channel widths are presented in Fig. 2 (reprinted from ref. 45, ref. 47 and 52). In all cases the drop size is comparable to the channel width, and the drops reside approximately in the midplane of the channel. We observe that, depending on the experimental conditions, the drops can either form "pearl-necklace" chains of closely spaced drops (Fig. 2(a)) or chains with a much larger drop separation (Fig. 2(b and c)). The chains can either be well ordered (Fig. 2(a and c)) or have numerous defects (Fig. 2(b)).

Fig. 3 shows typical microstructural irregularities and defects that are analyzed here using direct FD/FT simulations and a quasi-2D theoretical model of drop dynamics. These defects include y-shaped chain configurations, coexisting chains with dense and sparse particle spacing, and laterally oriented chain defects formed by extra particles hydrodynamically bound to a chain side.

3 Methods: formulation of theoretical models

3.1 Analysis of hydrodynamic mechanisms controlling formation of ordered microstructure

We propose that two fundamental hydrodynamic mechanisms are responsible for the observed drop ordering in a shear-driven confined drop monolayer. First, the quadrupolar Hele-Shaw scattered flow produced by individual drops drives the neighboring drops into alignment.[10] Second, the swapping[57] (reversing) trajectory mechanism controls drop separation within the flow-oriented chains by providing effective drop repulsion.

The quadrupolar interparticle interactions and swapping-trajectory effect stem from the corresponding confinement-induced features of the flow field

$$\mathbf{v}_1 = \dot{\gamma} z \hat{\mathbf{e}}_x + \delta \mathbf{v}_1 \quad (1)$$

produced by an individual drop in the imposed Couette flow

$$\mathbf{v}_0 = \dot{\gamma} z \hat{\mathbf{e}}_x \quad (2)$$

between two parallel walls. Here $\dot{\gamma}$ is the shear rate, $\hat{\mathbf{e}}_x$ is the unit vector in the flow direction, and z is the transverse coordinate normal to the walls (see Fig. 4 for notation and the system schematic). The imposed Couette flow (2) vanishes in the midplane of the channel $z = 0$, and the walls move in opposite directions.

The flow $\delta\mathbf{v}_1$, scattered by a drop, acts on the surrounding drops, producing relative drop motion and leading to the microstructural evolution of the drop distribution. Without interparticle hydrodynamic interactions all drops would move to the midplane of the channel due to deformation-induced migration away from the walls.[59–61] Since the drops then would be in the same flow-vorticity plane, there would be no relative particle motion.

Fig. 5 and 6 illustrate the key features of the velocity field (1) that are critical for generation of the observed chaining behavior of a drop monolayer. The numerical results presented were obtained using the FD/FT method, described in more details in Section 3.4.

Fig. 5(a) depicts the flow field (1) in the centerplane of the channel. The results show that this scattered flow has the characteristic four-fold symmetry of the Hele-Shaw quadrupole.[10] We recall that in the slit geometry, the 3D near-field flow generated by force multipoles induced on the particles decays exponentially to a quasi-2D Hele-Shaw flow pattern at large distances.[62,63] In the Couette flow, a 2D quadrupole is the leading-order contribution. Fig. 5(b) illustrates how the corresponding quadrupolar hydrodynamic interactions between drops drive chain formation and produce attraction between flow-aligned drops.

The effective hydrodynamic repulsion that controls drop spacing within flow-aligned chains stems from the swapping-trajectory effect, first demonstrated for confined rigid spheres,[57] and subsequently discussed for a variety of systems.[2,13,21,64–68] Fig. 6(a) shows the flow field in the flow-gradient plane (x,z) passing through the center of the drop. The flow pattern viewed in this plane exhibits reversing streamlines,[57,64–66] which are the cause of the swapping-trajectory repulsion. In Stokes flow, reversing streamlines stem from confinement;[57] at finite Reynolds numbers they can also arise as a result of inertial effects.[64]

As schematically depicted in Fig. 6(b), and quantitatively shown in Fig. 6(c) the reversing flow moves interacting drops away from the midplane of the channel onto opposite-directed streamlines, driving the drops apart. Unlike the corresponding behavior for rigid particles in Stokes flow, the swapping trajectory repulsion between deformable drops decays with interparticle distance. This is because after reaching a sufficient separation, drops move back towards the midplane of the channel due to deformation-induced hydrodynamic migration[13,59–61,69–72] (the self-centering effect).

We will call this behavior the damped swapping-trajectory effect. It has been shown that the decaying inter-drop effective repulsion, combined with the far-field quadrupolar attraction, results in a stable stationary drop distance l_{st} in a confined pair.[13,58,65] Our results show that this distance, attained in an isolated confined pair at long times (see Fig. 6(c)), plays a nontrivial role in the microstructural evolution. The effective hydrodynamic repulsion that results from the damped swapping-trajectory effect is quantitatively modeled in Section 3.3, and its influence on the dynamics of the drop monolayer is discussed in Section 4.

To examine the role and quantify the effect of the quadrupolar and swapping-trajectory interactions in the microstructural evolution, we introduce two simplified suspension-dynamics models. In the first one, the particles interact only *via* pair-additive quadrupolar flow fields, and in the second one both quadrupolar and swapping-trajectory interactions are included. In both models, drops reside close to the midplane of the channel because of deformation-induced self-centering; thus the models are quasi-2D.

3.2 Evaluation of the quadrupolar hydrodynamic interactions

As discussed in our previous publications,[10,62,63] the scattered flow far from a particle confined in a parallel-wall channel tends exponentially to a parabolic Hele-Shaw form driven by a 2D harmonic pressure distribution,

$$\delta \mathbf{v}_1 = -\frac{1}{8}\eta^{-1}(H-2z)(H+2z)\nabla \delta p_1(\boldsymbol{\rho}). \tag{3}$$

Here Z is the fluid viscosity, H is the channel width, and $\boldsymbol{\rho} = x\hat{\mathbf{e}}_x + y\hat{\mathbf{e}}_y$ is the lateral position with respect to the particle center. In the Hele-Shaw regime, the pressure field is independent of the transverse position z; thus the pressure perturbation $\delta p_1(\boldsymbol{\rho})$ and the flow field (3) can be represented using the 2D multipolar expansion.

Unlike the corresponding behavior in Poiseuille flow, in Couette flow (2) there is no dipolar contribution because of the fore-aft symmetry of the system. Therefore, the leading-order multipolar contribution is the Hele-Shaw quadrupole

$$\delta p_1(\boldsymbol{\rho}) = \dot{\gamma}\eta q p_q(\boldsymbol{\rho}) \tag{4}$$

where

$$p_q(\boldsymbol{\rho}) = -\frac{d^2\left(x^2-y^2\right)}{4\rho^4} \tag{5}$$

is the dimensionless quadrupolar pressure field, q is its dimensionless quadrupolar moment, $\rho = |\boldsymbol{\rho}|$, and d is the drop diameter.

Since the pressure gradient $\nabla\rho$ and particle velocity $\mathbf{U}$ in a parallel-wall channel satisfy the linear mobility relation

$$\mathbf{U} = -\eta^{-1}H^2\mu\nabla p \tag{6}$$

(where μ is a dimensionless mobility coefficient), the far-field interparticle hydrodynamic interactions have a structure consistent with the quadrupolar form of the scattered flow (3)–(5). Using (6) and the superposition approximation

$$p(\boldsymbol{\rho}_i) = \sum_{j \neq i} \delta p_1(\boldsymbol{\rho}_{ij}) \tag{7}$$

for the pressure at the position ρ_i of a particle i in a multiparticle system, we find the corresponding superposition relation for the velocity $\mathbf{U}_i$ of particle i

$$\mathbf{U}_i = \dot{\gamma} d Q \sum_{j \neq i} \mathbf{v}_{\mathrm{q}}(\boldsymbol{\rho}_{ij}), \tag{8}$$

where

$$\mathbf{v}_{\mathrm{q}}(\boldsymbol{\rho}) = d^3 \nabla \frac{\left(x^2 - y^2\right)}{4\rho^4} \tag{9}$$

is the normalized quadrupolar hydrodynamic-interactions field, and $\boldsymbol{\rho}_{ij} = \boldsymbol{\rho}_i - \boldsymbol{\rho}_j$ is the relative position of particles i and j.

The dimensionless quadrupolar moment $Q = \mu q (H/d)^2$ of the quadrupolar hydrodynamic interactions (8) depends on the capillary number Ca (and thus on drop deformation) and the confinement ratio H/d. It depends also on the Marangoni number in the presence of surfactant. Since, by symmetry, there is no quadrupolar moment for spherical particles, the Hele-Shaw quadrupolar interactions stem entirely from drop deformation and/or surfactant redistribution. We thus have $Q = O(\mathrm{Ca})$ in the small-deformation regime.

Quadrupolar-interactions model with excluded-volume repulsion.—Since attractive quadrupolar forces alone would quickly lead to particle overlaps, our quadrupolar approximation (8) is enhanced by adding a near-field repulsion $\boldsymbol{u}_R(\boldsymbol{\rho}_{ij})$,

$$\mathbf{U}_i = \dot{\gamma} d \sum_{i \neq j} \left[Q \mathbf{v}_{\mathrm{q}}(\boldsymbol{\rho}_{ij}) + \mathbf{u}_{\mathrm{R}}(\boldsymbol{\rho}_{ij}) \right], \tag{10}$$

where

$$\mathbf{u}_{\mathrm{R}}(\boldsymbol{\rho}) = -\nabla V(\rho) \tag{11}$$

is a gradient of a short range repulsion potential $V(\rho)$, which mimics near-field hydrodynamic repulsion of nearly touching drops. We call the system defined by eqn (10) the quadrupolar-interactions (QI) model.

In our simulations the excluded-volume interactions (11) are modeled using the generalized Yukawa potential

$$V(\rho) = A_0 \rho^{-m} \mathrm{e}^{-\kappa_0 \rho} \tag{12}$$

with $m = 8$ and $\kappa_0 d = 6$. The amplitude A_0 is determined from the normalization condition $Q\mathbf{v}_q(\hat{\mathbf{e}}_x) + \mathbf{u}_R(\hat{\mathbf{e}}_x) = 0$, corresponding to the balance between the quadrupolar and excluded volume contributions for a flow-oriented pair of drops at contact.

3.3 Evaluation of hydrodynamic repulsion resulting from the damped swapping-trajectory effect

The QI model described above plays only an auxiliary role in our analysis, because it does not include the swapping-trajectory repulsion. In this section we develop a more comprehensive model that includes both the quadrupolar and damped swapping-trajectory effects.

As explained in our previous studies,[57,67] the swapping-trajectory repulsion of the particles in an interacting pair *i, j* is caused by the wall reflection of the scattered flow produced by one particle towards the other particle. This reflected flow results in transverse displacements of the interacting particles into oppositely directed streamlines of the imposed Couette flow; the Couette flow (2) then drives the displaced particles apart. This mechanism is manifested in particle trajectories and in the reversing structure of streamlines surrounding a confined particle (see Fig. 6).

For deformable drops, the transverse cross-streamline migration velocity u_{iz} of drop *i* in a pair *i, j* has a two-drop and a single-drop contribution,

$$u_{iz}\left(\boldsymbol{\rho}_{ij}, z_i\right) = u_{iz}^{\mathrm{Sw}}\left(\boldsymbol{\rho}_{ij}\right) + u_{iz}^{\mathrm{c}}\left(z_i\right). \tag{13}$$

The first term $u_{iz}^{\mathrm{Sw}}\left(\boldsymbol{\rho}_{ij}\right)$ is the swapping-trajectory velocity that results from hydrodynamic interactions of drops *i* and *j*. This term is an odd function of the relative drop position $\boldsymbol{\rho}_{ij}$, and at the leading order it is independent of the drop deformation. The second term $u_{iz}^{\mathrm{c}}\left(z_i\right)$ is the deformation-induced single-particle migration velocity toward the center of the channel (the self-centering contribution).

For a given transverse position z_i, the applied Couette flow convects drop i with the velocity

$$\mathbf{u}_{\|i}^{\mathrm{sw}}\left(z_i\right) = \alpha\dot{\gamma} z_i \hat{\mathbf{e}}_x, \tag{14}$$

oriented in the flow direction *x*. The mobility coefficient α in eqn (14) accounts for the drop interaction with the walls.

To incorporate the 3D swapping-trajectory dynamics described by eqn (13) and (14) into a quasi 2D suspension model, we use a quasistatic approximation for drop migration in the transverse direction *z*. Accordingly, we assume that the *z*-position of drop i in an interacting pair of drops *i, j* can be determined by balancing the two-particle swapping and single-particle self-centering contributions in eqn (13),

$$u_{iz}^{\mathrm{SW}}\left(\boldsymbol{\rho}_{ij}\right) + u_{iz}^{\mathrm{c}}\left(z_i\right) = 0. \tag{15}$$

The transverse quasi-equilibrium position of drop i,

$$z_i = z_0\left(\boldsymbol{\rho}_{ij}\right), \tag{16}$$

is evaluated from the velocity balance (15) and inserted into eqn (14), which yields the quasistatic approximation

$$\mathbf{u}_{\|i}^{\mathrm{SW}}\left(\boldsymbol{\rho}_{ij}\right) = \alpha\dot{\gamma}z_0\left(\boldsymbol{\rho}_{ij}\right)\hat{\mathbf{e}}_x \tag{17}$$

for the 2D drop velocity $\mathbf{u}_{\|i}^{\mathrm{SW}}$ produced by the damped swapping-trajectory effect. The velocity (17) is oriented in the flow direction and always drives the drops apart.

To obtain a closed-form expression for the swapping-trajectory repulsion (17) we provide explicit relations for the drop-migration contributions in the transverse drift balance (15). Based on the observation that the displacement of the drops from the midplane position $z = 0$ is small (see the results shown in Fig. 6(c)), we assume the linear relation

$$u_{iz}^{\mathrm{c}}\left(z_i\right) = -\beta\dot{\gamma}z_i \tag{18}$$

for the deformation-induced migration velocity, where the proportionality coefficient $\beta = O(\mathrm{Ca}^2)$ depends on the capillary number and the confinement ratio H/d.

Based on the known far-field form of the reflected flow driving the transverse swapping drift near a planar wall,[67] using two-wall superposition assumption in the near-field region, and taking into account the exponential decay of non-Hele-Shaw flow components at large distances in a two-wall system,[62,63] we propose a simple phenomenological approximation

$$u_{iz}^{\mathrm{SW}}\left(\boldsymbol{\rho}_{ij}\right) = \dot{\gamma}dAu_0^{\mathrm{SW}}\left(\boldsymbol{\rho}_{ij}\right), \tag{19}$$

$$u_0^{\mathrm{SW}}(\boldsymbol{\rho}) = \frac{d^3x}{\left(1 + \mathrm{e}^{\kappa\left(\rho - \rho_0\right)}\right)\left(b^2 + \left|\rho\right|^2\right)^2} \tag{20}$$

for the hydrodynamically induced transverse drift, where A, k, ρ_0, and b are fitting parameters used to match direct simulation data. In particular, ρ_0 is the distance at which the transition occurs from the algebraic to exponential decay of the flow that produces the swapping-trajectory effect.

By combining relations (14)–(20) we obtain the quasi-2D model of the swapping-trajectory repulsion,

$$\mathbf{u}_{\|i}^{\mathrm{SW}}\left(\boldsymbol{\rho}_{ij}\right) = \dot{\gamma}dBu_0^{\mathrm{Sw}}\left(\boldsymbol{\rho}_{ij}\right)\hat{\mathbf{e}}_x, \tag{21}$$

where $B = A\alpha/\beta$. The swapping trajectory effect decays at large interparticle distances due to the deformation-induced self-centering of the drops between the channel walls. Therefore,

the swapping trajectory repulsion decays more rapidly in systems with large capillary numbers. This qualitative argument is consistent with the observation that since $\beta = O(\mathrm{Ca}^2)$ for small capillary numbers, we have $B = O(\mathrm{Ca}^2)$, which implies that the range of the swapping trajectory repulsion increases in a small-deformation limit.

The result described by eqn (20) and (21) has been derived for a single pair of interacting drops. In a multi-drop system, the swapping-trajectory interactions are obtained by the superposition of pairwise contributions. The superposition assumption does not introduce any additional approximations, because of linearity of relations (17) and (18).

Quadrupolar-interactions plus swapping-trajectory repulsion model.—The swapping-trajectory repulsion effect (21) is combined with the quadrupolar hydrodynamic interactions (10) to obtain a comprehensive quadrupolar-interactions plus swapping-trajectory repulsion (QI+STR) model, defined by the equation

$$\mathbf{U}_{\|i} = \dot{\gamma} d \sum_{i \neq j} \left[Q \mathbf{v}_{\mathrm{q}}(\boldsymbol{\rho}_{ij}) + B u_0^{\mathrm{sw}}(\boldsymbol{\rho}_{ij}) \hat{\mathbf{e}}_x + \mathbf{u}_{\mathrm{R}}(\boldsymbol{\rho}_{ij}) \right]. \tag{22}$$

As already discussed, the model also incorporates the near-field excluded-volume repulsion (11) to prevent configurations with overlapping drops. We note that, while the QI+STR model does not explicitly describe the drop shape, drop deformation is implicitly incorporated in the description through the values of the model parameters (as described below).

Along the flow direction x the quadrupolar hydrodynamic interaction $v_q(\rho_{ij})$ is attractive, and the damped swapping-trajectory interaction $u_0^{\mathrm{sw}}(\boldsymbol{\rho}_{ij})\hat{\mathbf{e}}_x$ is repulsive. For an isolated pair of drops, these interactions balance at a stable stationary distance l_{st}. Consistent with earlier analyses,[13,58] the particles in a pair achieve this separation at long times. The role of the pairwise stationary drop separation l_{st} in controlling drop spacing is discussed in Section 4.

3.4 Benchmark system used to test theoretical predictions

The role of the quadrupolar and swapping-trajectory interactions will be determined by comparing direct benchmark simulations obtained by the FD/FT method[58,73–78] to the corresponding results from the QI and QI+STR models. As illustrated in Fig. 4, the benchmark system consists of deformable drops confined between two parallel walls at the confinement ratio $H/d = 1.2$. The periodic boundary conditions are applied in the flow direction x and vorticity direction y.

We assume that the drops are surfactant free, the capillary number Ca = 0.125 is moderate, and the viscosity η of the drops and continuous phase is the same. The Reynolds number is small but finite, Re = 0.1. Here $\mathrm{Ca} = \eta\dot{\gamma}a/\sigma$, and $\mathrm{Re} = \rho_{\mathrm{f}}\dot{\gamma}a^2/\eta$, where σ is the interfacial tension between the drop and continuous-phase fluids, ρ_{f} is the mass density of the fluids (the same for drops and the continuous phase), and $a = d/2$ is the drop radius. The finite inertia has a discernible quantitative effect on the drop motion, but key hydrodynamic mechanisms of drop ordering and crucial phenomenological features of the structural evolution are unaffected.

The benchmark FD/FT simulations were performed for two area fractions of the drop monolayer, $\phi_A = 0.05$ and $\phi_A = 0.3$ (where $\phi_A = \frac{1}{4}\pi n d^2$, and $n = N/A$ is the number of drops per unit area). The results for $N = 76$ drops at area fraction $\phi_A = 0.05$ and $N = 456$ drops at $\phi_A = 0.3$ are presented in Fig. 7. At time $t = 0$ the drops were placed randomly in the midplane of the channel. The initial conditions, which were also used in our QI and QI+STR calculations, are depicted in Fig. 8.

According to our simulations, the average Taylor deformation parameter $D = (L - B)/(L + B)$ for drops in the system with area fraction $\phi_A = 0.05$, is D = 0.22 (here L and B are the major and minor axes of the drop). This is the same value as the one found for an isolated drop under identical flow conditions (see the image shown in Fig. 6(a)). At area fraction $\phi_A = 0.3$, the Taylor deformation parameter is slightly lower, $D = 0.21$. This very minor difference in D indicates that the drop shape is dominated by the applied flow; hydrodynamic interactions between drops do not affect the shape in a significant way.

The benchmark-simulation frames presented in Fig. 7 (also see ESI,† Movies M1 and M2) indicate that for both low and high area fractions the drops rapidly form a partially ordered flow-aligned drop-chain microstructure with a significant number of defects. At longer times the system slowly anneals, resulting in a gradually increasing order. As illustrated in Fig. 3, there are marked similarities between the direct-simulation results and the experimental images, which indicates that the benchmark FD/FT simulations were performed in an experimentally relevant regime.

Benchmark-system parameters for the QI and QI+STR models.—To directly compare the QI and QI+STR models to the benchmark FD/FT simulations, we need to evaluate the quadrupolar moment Q and the parameters of the swapping-trajectory repulsion to match the benchmark-system dynamics. The matching was performed based on an analysis of the relative drop velocity for a pair of drops in a periodic unit cell. The quadrupolar moment was evaluated from the far-field behavior of the direct-simulation data, and the parameters of the swapping-trajectory interactions were obtained from the intermediate and near-field results. Only drops aligned in the flow direction x were considered in the parameter evaluation process.

Details of our matching procedure are described in Appendix A, and the model parameters used in our QI and QI+STR simulations are listed in Table 1. The longitudinal pair correlation function and the nearest-neighbor distributions discussed in Sections 4.3 and 4.5 are calculated by averaging over 10 simulation runs for a system of 512 particles.

4 Results

In what follows we use our theoretical models to determine how the quadrupolar interactions and hydrodynamic swapping-trajectory repulsion control the structural evolution in a drop monolayer. We start our discussion by comparing the benchmark FD/FT simulations presented in Fig. 7 with the QI (Section 4.1) and QI+STR (Section 4.2) simulations

†Electronic supplementary information (ESI) available. See DOI: 10.1039/c9sm00536f

performed for exactly the same initial drop configurations (depicted in Fig. 8) and matched parameter values (as described in Appendix A).

4.1 Hele-Shaw quadrupolar interactions induce drop alignment

To differentiate the effects of the quadrupolar interactions (8) and the swapping-trajectory contribution (21), we first consider numerical predictions of our auxiliary QI model (10). The simulation frames shown in Fig. 9 indicate that even without the swapping-trajectory repulsion drops rapidly align to form chains along the flow direction. This behavior is consistent with experimental data and direct simulation results presented in Fig. 7. The QI model thus confirms that the quadrupolar interactions drive drops into flow-aligned chains.

Our simulations, however, also reveal that QI model is insufficient to reproduce correct interparticle spacing. The differences between the direct FD/FT and approximate QI simulations are especially striking at the low area fraction $\phi_A = 0.05$ (see Fig. 7(a) and 9(a)). According to the direct simulations the drops in already formed chains are sparsely spaced, with the center-to-center distance of approximately two particle diameters. In contrast, the QI simulations yield chains of touching particles; moreover these chains are more fragmented. The discrepancies between the direct and approximate quadrupolar simulations are less pronounced at $\phi_A = 0.3$ (see Fig. 7(b) and 9(b)), but clear differences in particle spacing and dissimilarities in the type and number of defects in the chain structure are still evident.

Our results thus indicate that an important factor that controls particle spacing is missing in the QI model. This factor—the swapping-trajectory mechanism—is discussed next.

4.2 A combination of quadrupolar and swapping-trajectory interactions governs morphological evolution

A comparison between the simulation images obtained using the rudimentary QI model (Fig. 9) and the more comprehensive QI+STR method (Fig. 10) shows that the damped swapping trajectory effect that gives rise to the hydrodynamic swapping-trajectory repulsion plays an important role in chain forming. Adding the swapping-trajectory repulsion to the quadrupolar model rectifies the particle spacing problem present in the QI simulations. We find that at the low area fraction $\phi_A = 0.05$ the QI+STR model yields uniform spacing within all chains. For $\phi_A = 0.3$ the spacing within individual chains is quite uniform, but there are significant spacing differences from chain to chain. These findings are consistent with the results of the direct FD/FT simulations depicted in Fig. 7.

According to Fig. 7(a) and 10(a), at $\phi_A = 0.05$, drop configurations in the direct and QI+STR simulations are nearly identical, provided that the timescale is adjusted by rescaling simulation time by a constant factor. In some cases the observed chain reconnections lead to a different chain topology or different relative timing of restructuring events. However, taking into account that particle trajectories in multiparticle systems are typically sensitive to small perturbations, the QI+STR model provides close to quantitative description of the drop dynamics. Therefore, the model correctly accounts for the microstructural evolution mechanisms in the far-field and intermediate-field regions.

At the higher area fraction $\varnothing_A = 0.3$, the QI+STR simulations do not reproduce individual drop arrangements, except at relatively short times (see the first two panels in Fig. 10(b)). A comparison of the systems at a similar evolution stage requires a more significant time-scale adjustment than the one needed for $\varnothing_A = 0.05$. Yet, the model provides good semi-quantitative agreement with the benchmark FD/FT simulations. In particular, in both systems presented in Fig. 7(b) and 10(b), the chains formed at the early stage of the evolution are wavy, branched, and disordered, and they gradually anneal into an increasingly ordered structure.

The time rescaling that is involved in matching the QI+STR model to the benchmark FD/FT simulations stems from the fact that the far-field quadrupolar interactions (9) overpredict relative particle motion at small and moderate interparticle distances. This overprediction is especially pronounced in the vorticity direction, where there is no compensating swapping-trajectory effect. Thus, particle ordering and subsequent restructuring of the chain configuration occur at earlier times in the QI+STR model than in the corresponding direct FD/FT simulations. The overall correct form of the quadrupolar streamlines, however, leads to correct predictions of the microstructural evolution.

We find that both, in the direct and QI+STR simulations, chains merge either by connecting their ends drawn together by the quadrupolar interactions (see Fig. 11) or by a zipping process depicted in Fig. 12. The zipping process dominates at high area fractions, and the end-to-end merging is more frequent at low drop concentrations.

In the following section we use long-time QI+STR simulations to determine mechanisms that control drop spacing and structural evolution in a well-developed chain microstructure.

4.3 Swapping-trajectory repulsion qualitatively alters drop spacing statistics

To characterize the shear-induced flow-oriented drop ordering at long times we consider the longitudinal pair correlation function

$$g_{\parallel}(\rho) = \langle g(\boldsymbol{\rho}) \rangle_{\theta}, \quad |\theta| \leq 15^{\circ}. \tag{23}$$

Here θ is the angle formed by the line of centers $\boldsymbol{\rho}$ with the flow direction, $\langle \cdot \rangle_{\theta}$ denotes angular averaging over all pairs forming angles in the specified range, and g($\boldsymbol{\rho}$) is the 2D pair correlation function. The cutoff angle $\theta = 15^{\circ}$ has been chosen based on typical chain orientations to include mostly pairs of drops belonging to the same chain and exclude pairs of drops from different chains.

The longitudinal pair correlation function (23) is depicted in Fig. 13 for several systems with a well-developed long-time chain microstructure. The left panels show the results of QI +STR calculations. To help elucidate the role of the swapping-trajectory repulsion, the right panels depict QI simulation results, for quadrupoles with no swapping-trajectory effect. The results are presented for low (top panels), intermediate (middle), and high area fractions (bottom).

The predictions of the QI+STR model show that at a low area fraction $\phi_A = 0.05$ (Fig. 13(a)) the function $g_{\parallel}(\rho)$ is sharply peaked. For an intermediate area fraction $\phi_A = 0.15$ (Fig. 13(b)), however, the peaks disappear, indicating an increased disorder. Yet, they reemerge at a high area fraction $\phi_A = 0.3$ (Fig. 13(c)), but with a smaller spacing. In contrast, in the absence of the swapping-trajectory repulsion there is no reemergent behavior of the peak structure, and the pair correlation function $g_{\parallel}(\rho)$ is always sharply peaked, with a fixed peak spacing approximately equal to the drop diameter d. The qualitatively distinct longitudinal correlations obtained from the more complete QI+STR and the rudimentary QI models reveal a nontrivial role of the swapping-trajectory interactions in controlling the particle distribution.

4.4 Drops within individual chains are equally spaced, but different chains can have different spacing

To further elucidate the statistics of drop spacing in the self-organized chain structure at long times, Fig. 14 presents the probability distribution $f_d(\rho/d)$ of the dimensionless drop-to-drop distance r/d for representative individual chains at the area fractions $\phi_A = 0.05$, 0.15, and 0.3. The chains for which the probability distribution is shown are marked in blue in the corresponding simulation images depicted above the plot. The results are presented both for fully equilibrated chains (left and middle panels) and unequilibrated chains (right panels).

We find that for all area fractions the probability-distribution peaks in fully equilibrated chains are sharp and equally spaced, which demonstrates that the drop spacing within the chains is uniform. The peaks in chains where drop spacing is affected by hydrodynamic interactions with other chains (see examples shown in the right panels of Fig. 14(b and c)) are broad, but well separated; they often have double- or triple-peak structure, indicating the existence of zones with different spacing. The peak structure in far-from-equilibrium chains that result from zipping is often irregular, which is due to a considerable drop spacing variation near the zipping region in the resultant chain (see the zipping example shown in Fig. 14(a)).

Consistent with a prediction of Sarkar and Singh,[58] we observe that at a low area fraction $\phi_A = 0.05$, i.e., in the regime where the chains are fragmented and do not strongly interact with each other, the peak spacing in equilibrated chains approximately equals the stationary spacing in an isolated pair of drops l_{st} (for parameters used in our simulations we have $l_{st}/d = 2.08$). In contrast, at higher area fractions, *i.e.*, under conditions for which the chains either span the entire system or strongly interact with other chains, the drop spacing is typically smaller than l_{st}. We find that for $\phi_A = 0.15$ drop spacing varies widely from chain to chain; and for $\phi_A = 0.3$ many neighboring chains are closely packed (with drop separation $\rho/d \approx 1$), although some chains have larger spacing.

Uncompressed and compressed chains.—The analysis presented above indicates that drop chains behave similarly to uncompressed and compressed chains of beads connected by identical springs. If a finite bead chain is free of external forces, all springs are fully relaxed to their equilibrium length. When the chain is infinite or compressive forces act

on the terminal beads, the bead spacing can be smaller than the equilibrium spring length, but under equilibrium conditions the spacing still remains uniform.

Based on this analogy, we refer to drop chains with the spacing $\rho \approx l_{st}$ as uncompressed, and $\rho < l_{st}$ as compressed (see the schematic shown in Fig. 15). Similar to the spring chains, finite equilibrated drop chains with free ends are uncompressed, because of the hydrodynamic force balance on the interior and terminal drops. Note that drop chains under tension above the stability threshold would get fragmented, because the hydrodynamic interactions weaken with the increasing drop distance (similar to springs softening under strain). Chains with spacing significantly larger than l_{st} thus do not form.

4.5 The observed drop-spacing characteristics are reflected in the first- and second-neighbor distance distributions

The observations presented in Section 4.4 are based on an examination of drop spacing in selected individual chains. Our conclusions, however, are also quantitatively confirmed by the statistical analysis of the first- and second-nearest neighbor-distances l_1 and l_2 in the drop monolayer.

Fig. 16(a) shows the probability distribution $f_1(l_1/d)$ for the normalized nearest-neighbor distance l_1/d, and Fig. 16(b) presents the probability distribution $f_{21}(l_2/l_1)$ for the ratio between the second- and first-nearest-neighbor distances. The function $f_1(l_1/d)$ provides statistical information regarding the spacing distribution for drops in all chains. In contrast, the function $f_{21}(l_2/l_1)$ characterizes the spacing uniformity within the chains by comparing the distances between a given drop and its left and right neighbor. Except for the terminal drops in a chain, the first- and second-nearest-neighbors are on the opposite sides of a given drop.

The results depicted in Fig. 16 indicate that the function $f_{21}(l_2/l_1)$ is sharply peaked at $l_2/l_1 = 1$ for all area fractions, confirming that drop spacing in individual chains is uniform. In contrast, the width of the nearest-neighbor distribution $f_1(l_1/d)$ strongly depends on the area fraction. The distribution is narrow and peaked at the stable pair separation $l_1 \approx l_{st}$ for $\phi_A = 0.05$, showing that at low area fractions the chains are mostly uncompressed. The peak is broad (spanning the range $d \lesssim l_1 \lesssim l_{st}$) for $\phi_A = 0.15$, indicating that the degree of compression of different chains varies. For $\phi_A = 0.3$, the peak narrows and shifts towards the drop contact distance, $l_1/d = 1$, which corresponds to the maximal chain compression.

This behavior of the nearest neighbor distributions is consistent with the observed spacing variation from chain to chain (see Fig. 14) and the reemergent peak structure of the pair distribution $g_{||}(\rho)$. The function $g_{||}(\rho)$ loses the oscillatory structure at $\phi_A = 0.15$ (see Fig. 13), because peaks originating from uniform spacing in individual chains are averaged out due to large chain-to-chain fluctuations. This averaging effect is weaker at low and high area fractions, because the chains are either uncompressed or maximally compressed.

4.6 Uncompressed chains grow by end-to-end merging, and compressed chains are produced *via* zipping

An examination of the results of the direct FD/FT and QI+STR simulations indicates that at low area fractions (see ESI,† Movies M1 and M3) annealing of the chain microstructure occurs primarily by merging of chain ends. This end-to-end connection process, illustrated in Fig. 11, does not produce chains with a reduced drop spacing (compared to l_{st}), i.e., chains remain uncompressed.

At higher area fractions (see ESI,† Movies M2 and M4) chain merging events occur mostly *via* a zipping process, in which two approximately parallel chains merge into a single chain with a smaller drop spacing. As depicted in Fig. 12, the original chains and the resulting chain usually form a y-shaped defect in the chain microstructure. The defect propagates when the drops from the two original chains are incorporated into the resulting chain either successively (one by one) or in groups of several.

Absorption in groups is found more frequently in the direct FD/FT simulations than in the QI+STR model (see ESI,† Movies M2 and M4). The existence of some differences in fine features of the zipping process in the direct and QI+STR simulations is expected because details of near-field effects are not included in the QI+STR model.

The role of quadrupolar interactions and swapping-trajectory repulsion in chain zipping.—Fig. 17 explains the hydrodynamic mechanism that drives chain zipping. Two important factors are here at play: the geometry of the superposition of the quadrupolar flow fields produced by the drops in the chain, and the anisotropy of the swapping-trajectory repulsion. The superposition flow initially aligns a new drop with the gap between two drops in a chain, and then drives the drop into the gap. The anisotropic swapping-trajectory repulsion does not hinder the particle incorporation process because this hydrodynamic force acts only in the flow direction x. The swapping-trajectory repulsion, however, contributes to the zipping process by redistributing drops in the chain and maintaining gaps between them.

We note that relaxation of density fluctuations in a drop chain is diffusive, similar to the relaxation of a fully overdamped spring-bead chain. This behavior is in contrast to the wave dynamics observed in chains of drops driven by confined Poiseuille flow.[40,42] In Poiseuille flow, the direction of the wave propagation is determined by the orientation of the pressure gradient; contrary to this behavior, the fore-aft symmetry of a sheared drop monolayer results in diffusive chain-relaxation processes.

A sequence of zipping events depends on the distribution of defects in the chain structure formed at the earlier stages of the system evolution. Thus, zipping produces a variety of compressed chains with different drop spacing. The zipping process terminates when most of the defects are annealed and the drops are arranged into a set of parallel percolating chains. At high area fractions, drop incorporation into a chain also terminates when a chain becomes closely spaced. This results in increased formation of laterally oriented chain defects, in which unabsorbed particles are hydrodynamically bound to a chain side (as illustrated in Fig. 3(c)).

We note that a soft isotropic repulsion force of the range approximately equal to the range of the swapping trajectory repulsion would significantly change the system dynamics by preventing chain zipping. As a result, at high area fractions chain restructuring would occur primarily by chain reconnection. In such a hypothetical system (see ESI,† Movie M8), an approximately hexagonal microstructure develops at long times, with a large number of defects.

5 Conclusions

Our study provides a detailed analysis of hydrodynamic mechanisms that govern the formation and subsequent evolution of self-organized chain-like structures in flow-driven drop monolayers in a narrow-gap Couette device. We explicitly demonstrate that experimentally observed spontaneous formation of flow-aligned chains of drops results from hydrodynamic interactions associated with Hele-Shaw quadrupolar scattered-flow patterns produced by individual drops, as predicted in our earlier study.[10] We also quantify the role of damped swapping-trajectory effect, which gives rise to swapping-trajectory repulsion that controls drop spacing.

We have developed a quasi-2D QI+STR theoretical model for description of the dynamics of a drop monolayer. The model combines evaluation of quadrupolar hydrodynamic interactions with a quasistatic approximation of the swapping-trajectory repulsion between deformable drops. The proposed approach provides accurate quantitative description of drop dynamics at low area fractions and semi-quantitative results at high area fractions. We also show that chains tend to have uniform spacing but this spacing varies from chain to chain because the swapping-trajectory hydrodynamic repulsion allows chains to be compressed as seen in our FD/FT and QI+STR simulations.

The QI+STR model is simple and easy to implement numerically for large multiparticle systems. It is particularly useful for exploring long-time evolution, because of prohibitive numerical cost of direct FD/FT simulations in the long-time regime. In our present study, the parameters of the model were determined from benchmark FD/FT direct simulations of a hydrodynamically coupled drop pair. A similar methodology can also be applied for other systems, with different capillary numbers, wall separations, and for different kinds of deformable particles (including surfactant-covered drops and non-Newtonian drops in a Newtonian fluid). The model can also be used to examine the role of stable pair separation for an interacting drop pair.

Based on both FD/FT and QI+STR simulations, we observe that at low area fractions drop spacing in all chains is approximately the same and equals the stable pair separation l_{st}. In contrast, at higher area fractions there is a significant spacing variation from chain to chain. This behavior can been explained using concepts of uncompressed and compressed chains. Equilibrated chains with free ends are uncompressed and have the spacing l_{st}; percolating chains or chains with ends anchored at microstructural defects are usually compressed and have smaller spacing. The compressed chains are usually formed by chain zipping, and uncompressed ones by end-to-end merging.

We note that, while drop coalescence is not incorporated in our model, the identified factors that control drop spacing are relevant for systems of coalescing drops. Most dramatically the coalescence occurs in the transient process in which drops in already formed chains merge into elongated fluid strings.[5,45] Our study yields useful insights into the behavior of such systems, by describing mechanisms of the initial drop ordering and the subsequent evolution of drop spacing before the coalescence into strings takes place.

The hydrodynamic mechanisms and structural relaxation processes analyzed in this study for a shear-driven drop monolayer are likely to be also relevant for other flow-driven systems of deformable particles under confinement. For example, related hydrodynamic phenomena have recently been discussed for a shear-driven red blood cell (RBC) monolayer.[13] Continuous and fragmented particle chains with different spacing have been observed for RBCs in a capillary,[79] and for drops in inertial microfluidic systems.[2,23] Spacing variation in such chains and a threshold for chain fragmentation can be analyzed not only in terms of the pairwise stationary separation l_{st} but also chain compression.

Spontaneous emergence of chain-like structures also occurs in shear-driven suspensions of rigid spheres dispersed in non-Newtonian fluids,[80–84] especially under confinement.[83] We surmise that flow fields of a similar symmetry to the ones considered herein are responsible for particle chaining in such systems, with nonlinear suspending fluid rheology having a role analogous to drop deformation. In particular, nonlinear second-order perturbation produces quadrupolar scattered flow pattern around spherical particles, due to coupling properties of spherical harmonics and the symmetry of the imposed shear flow. Moreover, since swapping trajectories do not require deformation, and particles in non-Newtonian fluids are self-centering, rigid spheres in confined non-Newtonian fluids are subject to the swapping-trajectory repulsion.

Our findings, therefore, are likely to have broad implications for flow-driven microstructure formation in complex media. The theoretical insights and the QI+STR simulation framework developed in our study are relevant for a variety of flow-driven systems where quadrupolar backflow patterns organize particles into chains, and anisotropic flow-oriented particle repulsion affects particle spacing.

Supplementary Material

Refer to Web version on PubMed Central for supplementary material.

Acknowledgements

J. B. and S. S. were supported by NSF Grant CBET 1603627. They also acknowledge TTU HPCC, whose computational resources were used to perform QI and QI+STR simulations. The FD/FT numerical simulations were performed, in part, on the Colonial One cluster at The George Washington University. This work used the Extreme Science and Engineering Discovery Environment (XSEDE), which is supported by NSF grant number ACI-1548562. Specifically, the Comet Supercomputer at the San Diego Supercomputer Center was used. M. L. was supported by NSF Grant CBET 1603806.

Appendix A:: evaluation of parameters of the QI and QI+STR models

In this Appendix we evaluate the quadrupolar moment Q and the parameters of the swapping-trajectory repulsion defined by eqn (20) and (21) for the benchmark system introduced in Section 3.4. The parameters are determined from an analysis of the time evolution of a periodic system with two drops in a unit cell. Since the direct FD/FT simulations require discretization of the entire fluid domain, the size of the unit cell is limited by the numerical cost. Thus, the parameter-matching procedure was performed in a relatively small unit cell with dimensions $23.04d \times 3.84$d in the flow and vorticity directions, respectively.

In such a small cell, the particle interactions with their images cannot be neglected. Therefore, fitting of the model parameters was performed in QI and QI+STR systems with the same periodicity as the direct-simulation unit cell. The periodic quadrupolar interactions were evaluated using Ewald-summation techniques, and the swapping-trajectory interactions by direct summation in real space.

Appendix A.1: evaluation of the quadrupolar moment

The quadrupolar moment Q was determined from an analysis of the drop velocity for large drop separations, *i.e.*, in the regime where the quadrupolar interactions dominate the system behavior. In the direct simulations, the velocity was obtained from a single long simulation run for a pair of drops 1, 2 aligned in the flow direction, *i.e.*, a pair with the relative drop position $\boldsymbol{\rho}_{12} = x_{12}\hat{\mathbf{e}}_x$ in the flow-vorticity plane. The initial drop separation was $x_{12}/d = 4$, and the drops were placed in the midplane of the channel.

Fig. 18 presents the normalized longitudinal velocity

$$\overline{U}_{1x} = (\dot{\gamma}d)^{-1} U_{1x} \tag{24}$$

of drop 1 along the trajectory. The direct numerical simulations are compared with the quadrupolar velocity (8) evaluated for the same system. The value of the quadrupolar moment is obtained from the relation

$$Q = \overline{U}_{1x}/v_{\mathrm{q}x}^{\mathrm{per}}, \quad x_{12}/d \gg 1, \tag{25}$$

where $v_{\mathrm{q}x}^{\mathrm{per}}$ is the normalized quadrupolar hydrodynamic-interaction field (9) summed over the periodic images. A good quantitative fit is obtained for the quadrupolar moment $Q = 0.09 \pm 0.01$ (see the inset of Fig. 18). In our QI and QI+STR models we use $Q = 0.096$, for which the value of the direct simulations and QI results agree over a wider range of drop separations.

A relatively large numerical uncertainty of the quadrupolar moment Q stems from the fact that the relative drop velocity at large distances is much smaller than a typical fluid velocity $\dot{\gamma}d$. Hence, a significant numerical noise.

Appendix A.2: evaluation of parameters of the model

The results depicted in Fig. 18 show that for $x_{12}/\lesssim$ t 2.6, the drop velocity significantly differs from the quadrupolar far-field result. The drop velocity $\bar{U}$ reaches a maximal magnitude at x_{12}/d ≈ 2.4 and decreases to zero at

$$x_{12}/d \approx 2.17, \tag{26}$$

which is a stable stationary separation for a pair of drops in the periodic cell. In contrast, the quadrupolar field (9) is monotonic and smaller than zero for all drop separations along the flow direction *x*.

The behavior of the drop velocity on the approaching-drop trajectory shown in Fig. 18 can be quantitatively described using a combination of the quadrupolar interactions and swapping-trajectory repulsion defined in eqn (20) and (21). The quantitative fit of the model equations to the direct simulation results is represented in Fig. 18 by the dashed line.

The trajectory considered in Fig. 18 does not continue beyond the stationary separation (26). To represent the drop behavior for smaller values of x_{12}/d, we analyze several drop trajectories with the initial conditions in the range $1 < x_{12}/d < 1.5$. In all simulation runs the drops are initially spherical and placed in the midplane of the channel. The trajectories, shown in Fig. 19, indicate that drops with smaller initial separations have larger relative velocities, which stems from a larger transverse drop displacement at the beginning of the trajectory.

To approximate drop evolution using the quasistatic swapping-trajectory model, we choose the fitting parameter values that provide an overall qualitative agreement with the direct-simulation trajectories (see Fig. 19). A full quantitative agreement cannot be obtained within the quasi-2D QI+STR model because of limitations inherent in the quasistatic-balance assumption for the transverse drift (15).

To determine the parameters of the QI+STR model, we applied an iterative fitting procedure in which the amplitude B and the exponential-decay parameter κ were adjusted to match the drop velocity for x_{12}/d at and above the stationary separation (26), and the shift parameters b andρ_0 were used to control the velocity for smaller drop separations. The parameter values employed in our simulations are listed in Table 1.

References

1. Di Carlo D, Irimia D, Tompkins RG and Toner M, Proc. Natl. Acad. Sci. U. S. A, 2007, 104, 18892–18897. [PubMed: 18025477]
2. Humphry K, Kulkarni P, Weitz D, Morris J and Stone H, Phys. Fluids, 2010, 22, 081703.
3. Gallier S, Lemaire E, Lobry L and Peters F, J. Fluid Mech, 2016, 799, 100–127.
4. Uspal WE and Doyle PS, Soft Matter, 2014, 10, 5177–5191. [PubMed: 24913768]
5. Migler KB, Phys. Rev. Lett, 2001, 86, 1023–1026. [PubMed: 11178000]
6. Thorsen T, Roberts RW, Arnold FH and Quake SR, Phys. Rev. Lett, 2001, 86, 4163–4166. [PubMed: 11328121]

7. Link DR, Anna SL, Weitz DA and Stone HA, Phys. Rev. Lett, 2004, 92, 054503. [PubMed: 14995311]
8. Bonthuis DJ, Meyer C, Stein D and Dekker C, Phys. Rev. Lett, 2008, 101, 108303. [PubMed: 18851263]
9. Hashimoto M, Garstecki P, Stone H and Whitesides G, Soft Matter, 2008, 4, 1403–1413.
10. Janssen PJA, Baron MD, Anderson PD, Blawzdziewicz J, Loewenberg M and Wajnryb E, Soft Matter, 2012, 8, 7495–7506.
11. Caserta S and Guido S, Langmuir, 2012, 28, 16254–16262. [PubMed: 23134311]
12. Lee C-P, Lan T-S and Lai M-F, J. Appl. Phys, 2014, 115, 17B527.
13. Shen Z, Fischer TM, Farutin A, Vlahovska PM, Harting J and Misbah C, Phys. Rev. Lett, 2018, 120, 268102. [PubMed: 30004752]
14. Grzybowski BA, Stone HA and Whitesides GM, Nature, 2000, 405, 1033–1036. [PubMed: 10890439]
15. Lenz P, Joanny JF, Julicher F and Prost J, Phys. Rev. Lett, 2003, 91, 108104. [PubMed: 14525512]
16. Voth GA, Bigger B, Buckley MR, Losert W, Brenner MP, Stone HA and Gollub JP, Phys. Rev. Lett, 2002, 88, 234301. [PubMed: 12059365]
17. Riedel IH, Kruse K and Howard J, Science, 2005, 309, 300–303. [PubMed: 16002619]
18. Lenz P and Ryskin A, Phys. Biol, 2006, 3, 285–294. [PubMed: 17200604]
19. Underhill PT, Hernandez-Ortiz JP and Graham MD, Phys. Rev. Lett, 2008, 100, 248101. [PubMed: 18643631]
20. Tsang ACH, Shelley MJ and Kanso E, Soft Matter, 2018, 14, 945–950. [PubMed: 29319100]
21. Lee W, Amini H, Stone H and Di Carlo D, Proc. Natl. Acad. Sci. U. S. A, 2010, 107, 22413–22418. [PubMed: 21149674]
22. Morris JF, J. Fluid Mech, 2016, 792, 1–4.
23. Gao Y, Magaud P, Baldas L, Lafforgue C, Abbas M and Colin S, Microfluid. Nanofluid, 2017, 21, 154.
24. Kumnorkaew P, Ee Y-K, Tansu N and Gilchrist JF, Langmuir, 2008, 24, 12150–12157. [PubMed: 18533633]
25. Kamada A, Mittal N, Soderberg LD, Ingverud T, Ohm W, Roth SV, Lundell F and Lendel C, Proc. Natl. Acad. Sci. U. S. A, 2017, 114, 1232–1237. [PubMed: 28123065]
26. Kharchenko S, Douglas J, Obrzut J, Grulke E and Migler K, Nat. Mater, 2004, 3, 564–568. [PubMed: 15273745]
27. Obrzut J, Douglas JF, Kharchenko SB and Migler KB, Phys. Rev. B: Condens. Matter Mater. Phys, 2007, 76, 195420.
28. Huang J, Zhu Y, Jiang W, Yin J, Tang Q and Yang X, ACS Appl. Mater. Interfaces, 2014, 6, 1754–1758. [PubMed: 24397535]
29. Mao C, Huang J, Zhu Y, Jiang W, Tang Q and Ma X, J. Phys. Chem. Lett, 2013, 4, 43–47. [PubMed: 26291209]
30. Erni P, Cramer C, Marti I, Windhab E and Fischer P, Adv. Colloid Interface Sci, 2009, 150, 16–26. [PubMed: 19481192]
31. He Y, Huang Y, Li Q, Mei Y, Kong M and Yang Q, Colloid Polym. Sci, 2012, 290, 997–1004.
32. Gueron S, LevitGurevich K, Liron N and Blum J, Proc. Natl. Acad. Sci. U. S. A, 1997, 94, 6001–6006. [PubMed: 9177158]
33. Lenz P, Joanny J, Julicher F and Prost J, Eur. Phys. J. E: Soft Matter Biol. Phys, 2004, 13, 379–390.
34. Migler K, J. Rheol, 2000, 44, 277–290.
35. Blawzdziewicz J, Goodman RH, Khurana N, Wajnryb E and Young Y-N, Phys. D, 2010, 239, 1214.
36. Cheng X, Xu X, Rice SA, Dinner AR and Itai C, Proc. Natl. Acad. Sci. U. S. A, 2012, 109, 63–69. [PubMed: 22198839]
37. Blawzdziewicz J and Wajnryb E, J. Phys.: Conf. Ser, 2012, 392, 012008.
38. Cui B, Diamant H, Lin B and Rice SA, Phys. Rev. Lett, 2004, 92, 258301. [PubMed: 15245065]

39. Garstecki P, Nat. Phys, 2006, 2, 733–734.
40. Beatus T, Tlusty T and Bar-Ziv R, Nat. Phys, 2006, 2, 743–748.
41. Beatus T, Tlusty T and Bar-Ziv R, Phys. Rev. Lett, 2007, 99, 124502. [PubMed: 17930508]
42. Baron M, Bławzdziewicz J and Wajnryb E, Phys. Rev. Lett, 2008, 100, 174502. [PubMed: 18518295]
43. Shani I, Beatus T, Bar-Ziv RH and Tlusty T, Nat. Phys, 2014, 10, 140–144.
44. Ganan-Calvo A and Gordillo J, Phys. Rev. Lett, 2001, 87, 274501. [PubMed: 11800883]
45. Pathak JA, Davis MC, Hudson SD and Migler K, J. Colloid Interface Sci, 2002, 255, 391–402. [PubMed: 12505088]
46. Son Y, Martys N, Hagedorn J and Migler K, Macromolecules, 2003, 36, 5825–5833.
47. Pathak J and Migler KB, Langmuir, 2003, 19, 8667–8674.
48. Anna S, Bontoux N and Stone H, Appl. Phys. Lett, 2003, 82, 364–366.
49. Montesi A, Pena A and Pasquali M, Phys. Rev. Lett, 2004, 92, 058303. [PubMed: 14995347]
50. Garstecki P and Whitesides GM, Phys. Rev. Lett, 2006, 97, 024503. [PubMed: 16907453]
51. Hashimoto M, Mayers B, Garstecki P and Whitesides GM, Small, 2006, 2, 1292–1298. [PubMed: 17192976]
52. Vananroye A, Van Puyvelde P and Moldenaers P, Langmuir, 2006, 22, 2273. [PubMed: 16489817]
53. Van Puyvelde P, Vananroye A, Cardinaels R and Moldenaers P, Polymer, 2008, 49, 5363.
54. Tufano C, Peters GWA and Meijer HEH, Langmuir, 2008, 24, 4494–4505. [PubMed: 18348582]
55. Mao C, Huang Y, Yang J, Kong M, Wang Y, Yang Q and Li G, Langmuir, 2017, 33, 10577–10587. [PubMed: 28930633]
56. Singha S, Zurita-Gotor M, Loewenberg M, Migler K and Blawzdziewicz J, Bull. Am. Phys. Soc, 2017, 62, Q13.00002.
57. Zurita-Gotor M, Bławzdziewicz J and Wajnryb E, J. Fluid Mech, 2007, 592, 447–469.
58. Sarkar K and Singh RK, Phys. Fluids, 2013, 25, 051702.
59. Chan PC and Leal LG, J. Fluid Mech, 1979, 92, 131–170.
60. Chan PCH and Leal LG, Int. J. Multiphase Flow, 1981, 7, 83–99.
61. Smart JR and Leighton DT, Phys. Fluids A, 1991, 3, 21–28.
62. Bhattacharya S, Bławzdziewicz J and Wajnryb E, J. Comput. Phys, 2006, 212, 718–738.
63. Bhattacharya S and Bławzdziewicz J, J. Chem. Phys, 2008, 128, 214704. [PubMed: 18537444]
64. Kulkarni PM and Morris JF, J. Fluid Mech, 2008, 596, 413.
65. Doddi SK and Bagchi P, Int. J. Multiphase Flow, 2008, 34, 375–392.
66. Olapade PO, Singh RK and Sarkar K, Phys. Fluids, 2009, 21, 063302.
67. Zurita-Gotor M, Bławzdziewicz J and Wajnryb E, Phys. Rev. Lett, 2012, 108, 068301. [PubMed: 22401126]
68. Chiu S-H, Pan T-W and Glowinski R, Comput. Fluids, 2018, 172, 661–673.
69. Imaeda T, Physica A, 2000, 285, 306–314.
70. Mukherjee S and Sarkar K, J. Fluid Mech, 2013, 727, 318–345.
71. Singh RK, Li X and Sarkar K, J. Fluid Mech, 2014, 739, 421–443.
72. Mukherjee S and Sarkar K, Phys. Fluids, 2014, 26, 103102.
73. Sarkar K and Schowalter WR, J. Fluid Mech, 2001, 436, 177–206.
74. Tryggvason G, Bunner B, Esmaeeli A, Juric D, Al-Rawahi N, Tauber W, Han J, Nas S and Jan Y-J, J. Comput. Phys, 2001, 169, 708–759.
75. Li X and Sarkar K, Phys. Fluids, 2005, 17, 027103.
76. Li X and Sarkar K, J. Rheol, 2005, 49, 1377–1394.
77. Li X and Sarkar K, J. Fluid Mech, 2006, 564, 1–23.
78. Srivastava P, Malipeddi AR and Sarkar K, J. Fluid Mech, 2016, 805, 494–522.
79. McWhirter JL, Noguchi H and Gompper G, Proc. Natl. Acad. Sci. U. S. A, 2009, 106, 6039–6043. [PubMed: 19369212]

80. Pasquino R, Snijkers F, Grizzuti N and Vermant J, Langmuir, 2010, 26, 3016–3019. [PubMed: 20131839]

81. Pasquino R, Panariello D and Grizzuti N, J. Colloid Interface Sci, 2013, 394, 49–54. [PubMed: 23266026]

82. de Oliveira ISS, den Otter WK and Briels WJ, EPL, 2013, 101, 28002.

83. Van Loon S, Fransaer J, Clasen C and Vermant J, J. Rheol, 2014, 58, 237–254.

84. Pasquino R, D'Avino G, Maffettone PL, Greco F and Grizzuti N, J. Non-Newtonian Fluid Mech, 2014, 203, 1–8.

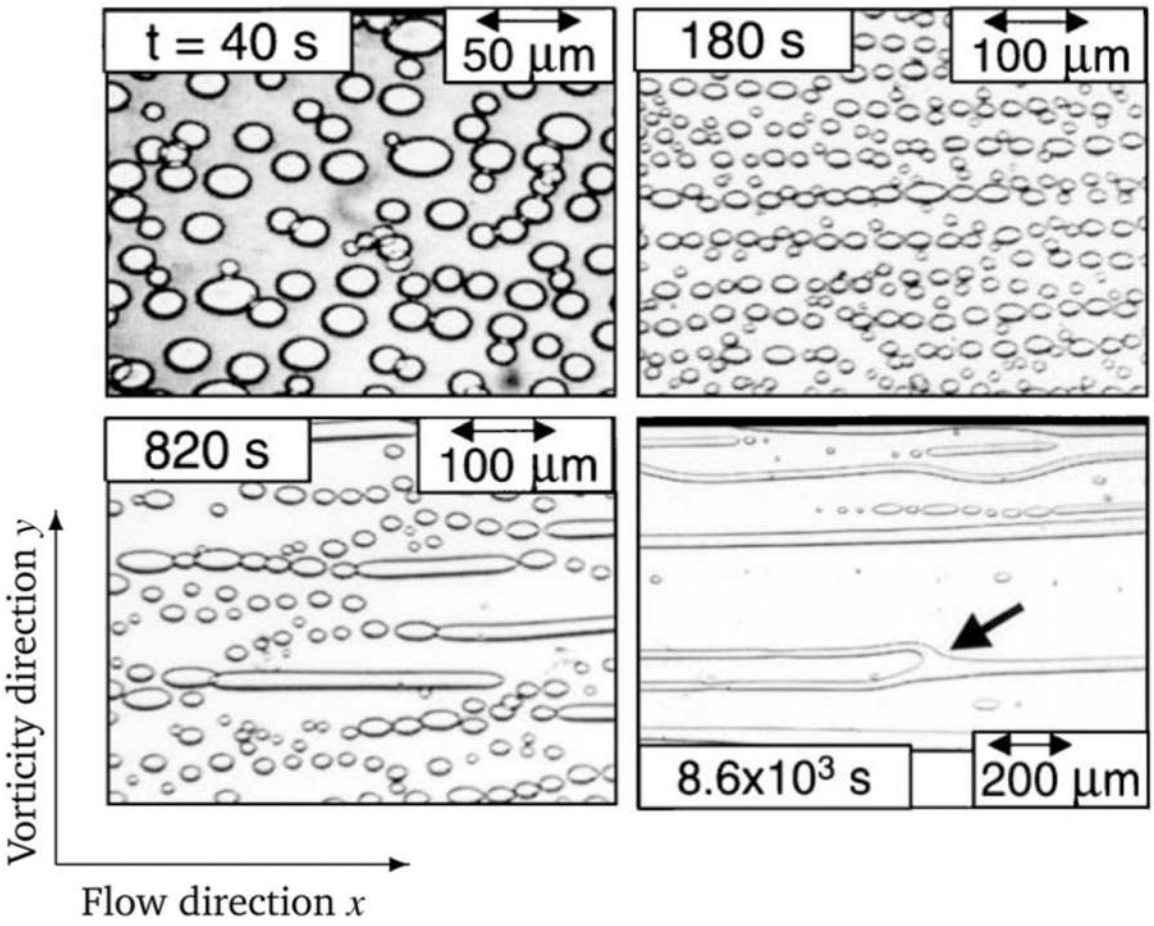

Fig. 1.

Self-assembly of flow-oriented structures in a strongly confined drop monolayer in Couette flow. The experimental images show that an initially disordered system (time $t = 40$ s) spontaneously self-organizes into drop chains ($t = 180$ s); chain formation is followed by drop coalescence ($t = 820$ s), which ultimately gives rise to emergence of ribbon-like structures at very long times ($t = 8.6 \times 10^3$ s). Images reprinted from ref. 5. Flow and vorticity directions as indicated.

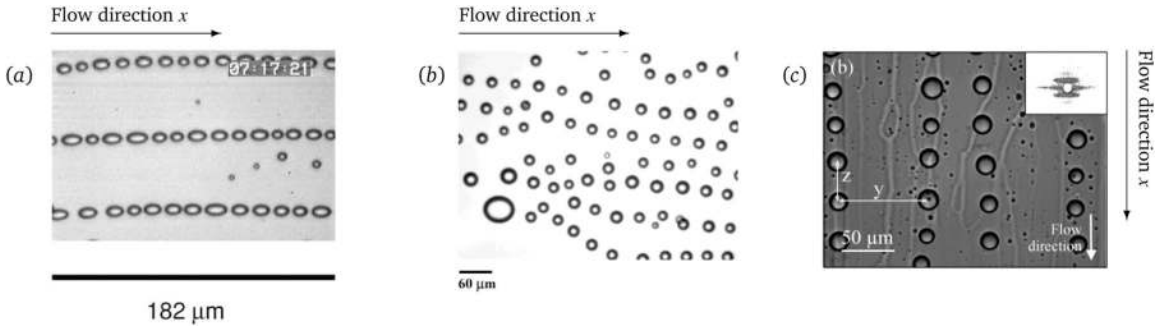

Fig. 2.

Examples of experimentally observed self-organized drop-chain structures. (a) Tightly spaced pearl-necklace chains; (b) sparsely spaced chains with a large number of defects; (c) well-organized sparsely spaced chains. Images reprinted from (a) ref. 45, (b) ref. 47, and (c) ref. 52. Flow direction as indicated.

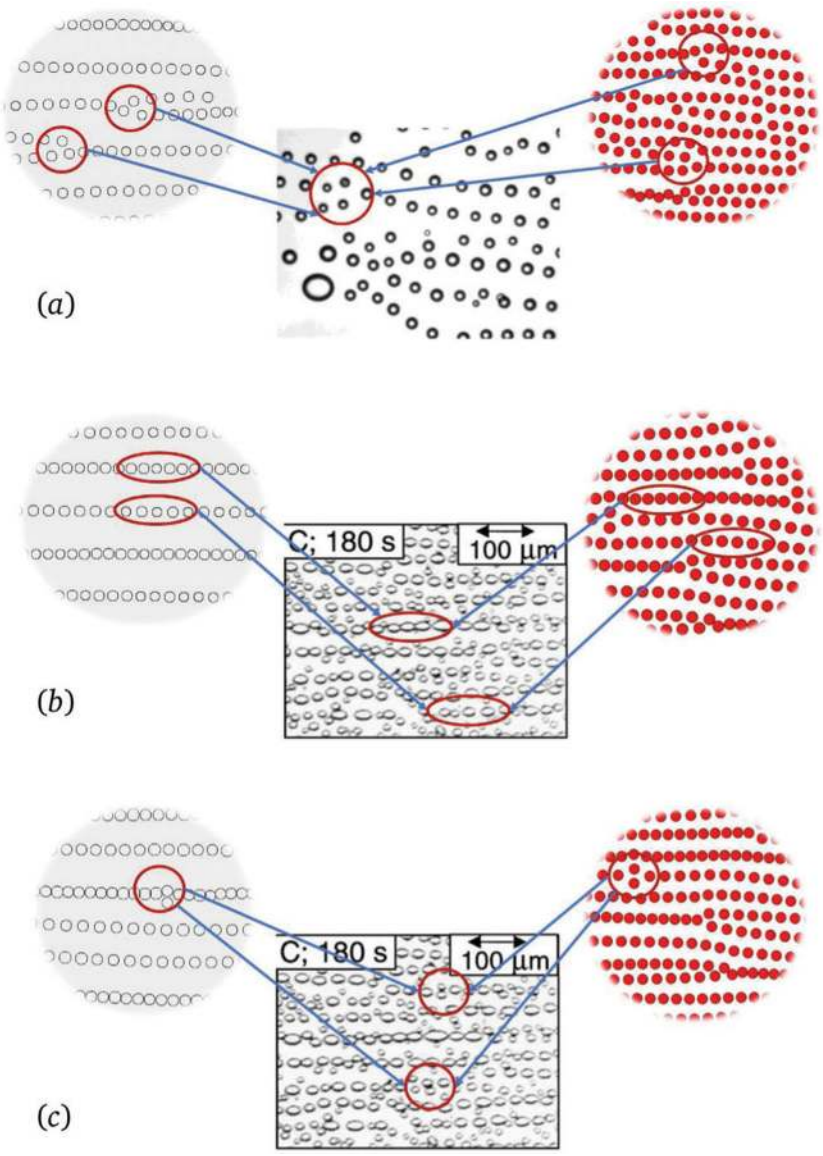

Fig. 3.

Typical defects in the chain microstructure of a shear-driven drop monolayer. Middle panels show experimental images, right panels direct numerical simulations, and left panels the results of a quasi-2D model, developed in Section 3.3, that includes quadrupolar interactions plus swapping trajectory repulsion (QI+STR model). (a) y-shaped defects associated with chain zipping; (b) common pattern of coexisting high-density and low-density chains observed at long times; and (c) laterally oriented chain defects. Experimental image (a) reprinted from ref. 47 and experimental images (b) and (c) reprinted from ref. 5. The flow direction x is horizontal, and vorticity direction y is vertical.

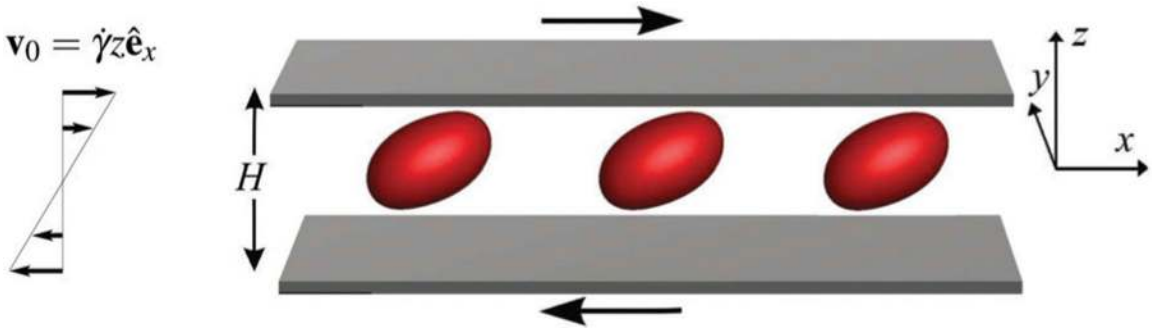

Fig. 4.

System schematic. A monolayer of deformable drops undergoes Couette flow between two parallel walls. The plane $z = 0$ is the midplane of the channel, and x is the flow direction.

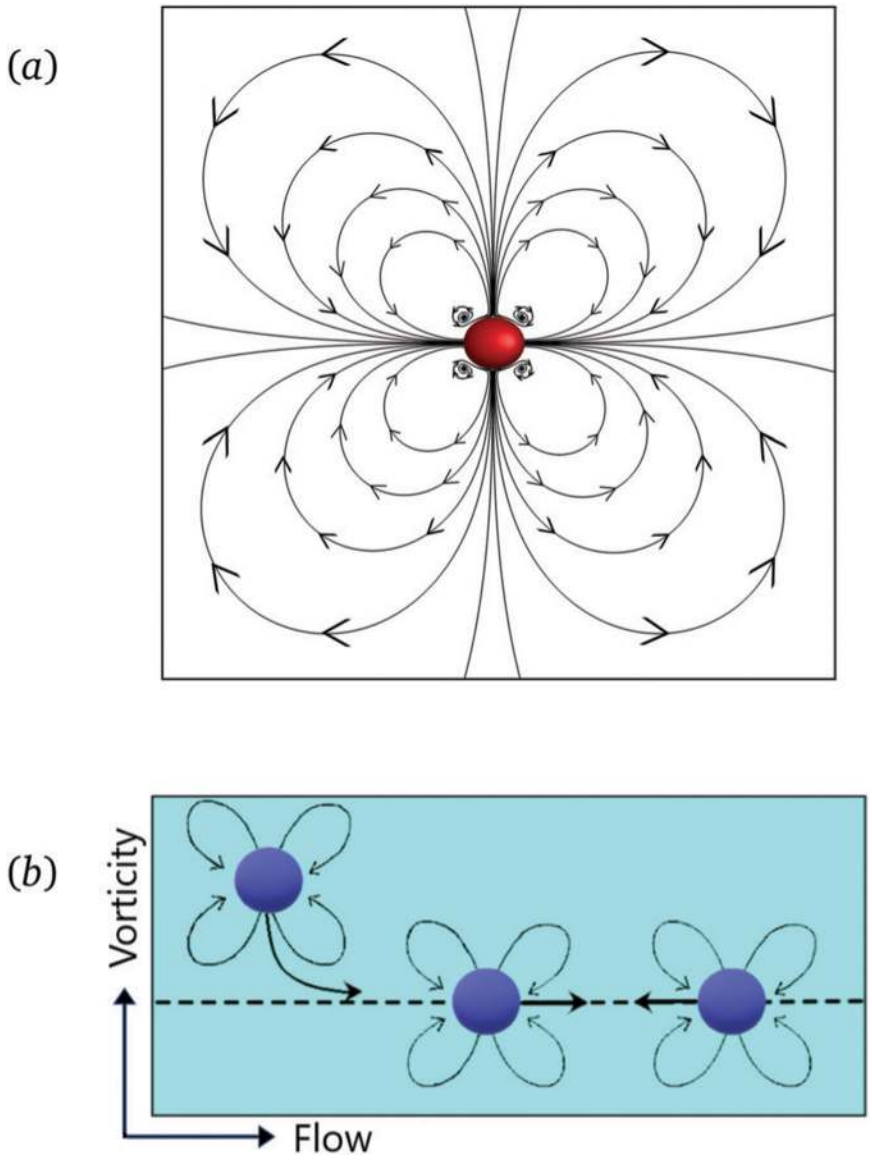

Fig. 5.

Quadrupolar mechanism of drop alignment. (a) Flow streamlines in the midplane of a channel for a single confined drop in the imposed Couette flow (2) (direct FD/FT simulations). The flow has a fourfold symmetry characteristic of the quadrupolar Hele-Shaw flow. (b) The mechanism by which Hele-Shaw quadrupolar interactions drive drops into alignment and produce inter-drop attraction oriented in the direction of the imposed flow.

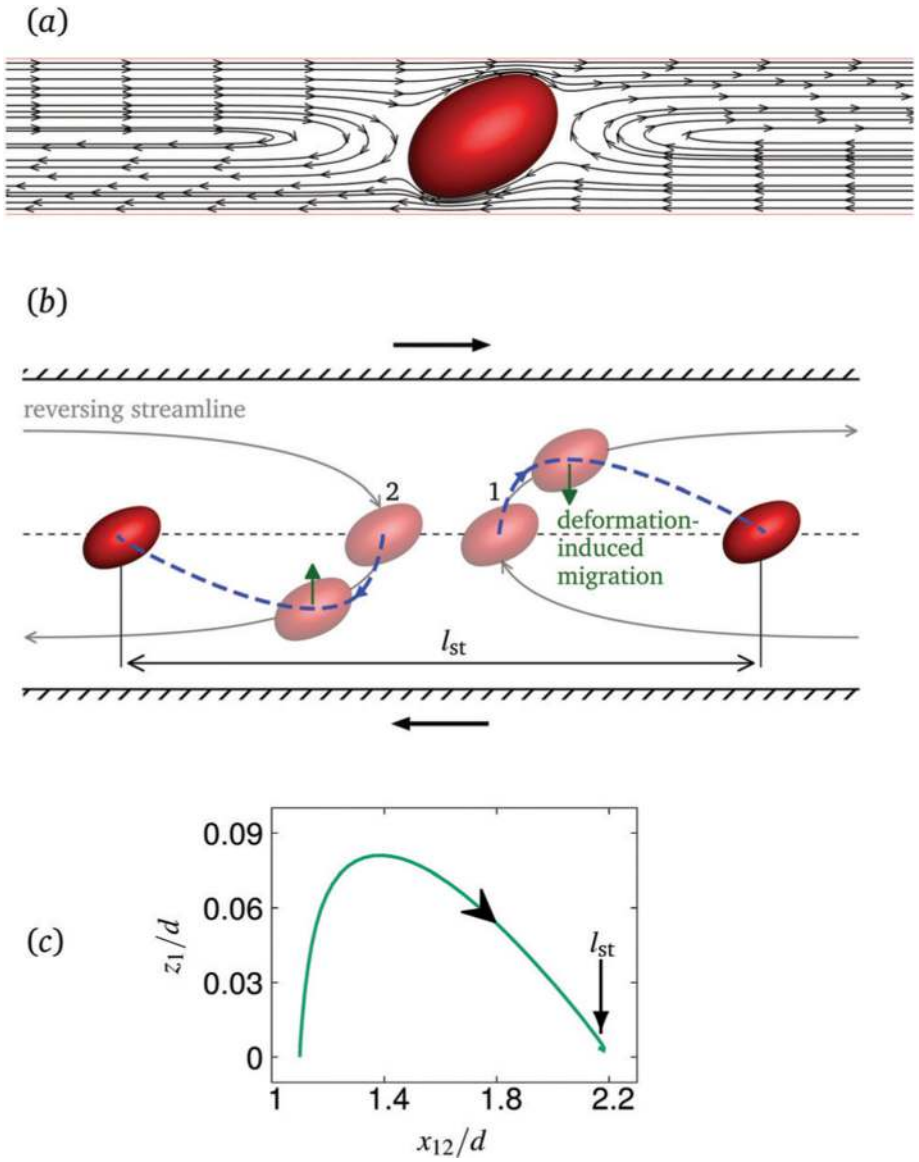

Fig. 6.

Mechanism of the swapping-trajectory repulsion for deformable drops in Couette flow. (a) Streamlines in the flow-gradient plane (*x,z*) for a single confined drop in the imposed Couette flow (2); the result obtained from FD/FT simulation. (b) Schematic explaining the swapping trajectory repulsion. Pink drops represent the initial and intermediate configurations; the long-time drop positions at the stable stationary separation l_{st} are shown in red. Deformation-induced drop migration towards the midplane of the channel is indicated by green arrows. The figure is not to scale. (c) FD/FT simulation results for the trajectory of drop 1 in a pair of drops initially aligned along the axis *x* (in the midplane of the channel). The graph shows the transverse displacement z_1 of drop 1 *vs.* relative drop separation x_{12} in the flow direction. The pairwise stable stationary separation l_{st} is indicated.

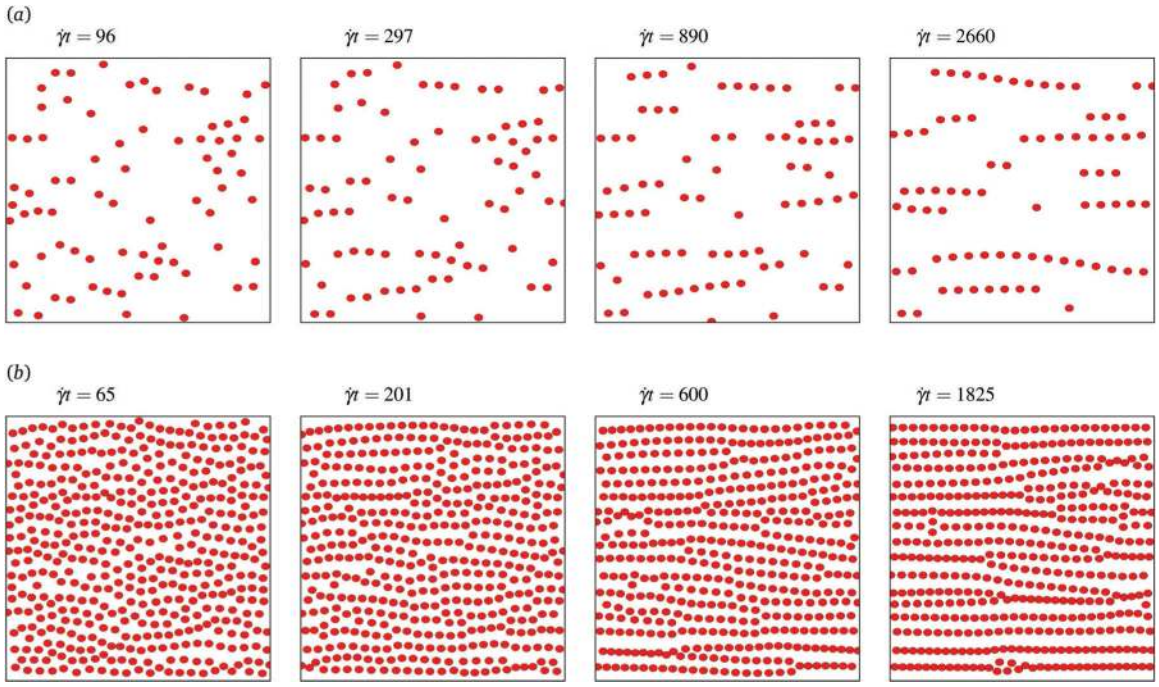

Fig. 7.

Benchmark FD/FT simulations of a strongly confined monolayer of drops in Couette flow. System evolution is shown for area fraction (a) $\phi_A = 0.05$ and (b) $\phi_A = 0.3$ (also see ESI,† Movies M1 and M2). The random initial configurations are depicted in Fig. 8, and system parameters are listed in Section 3.4.

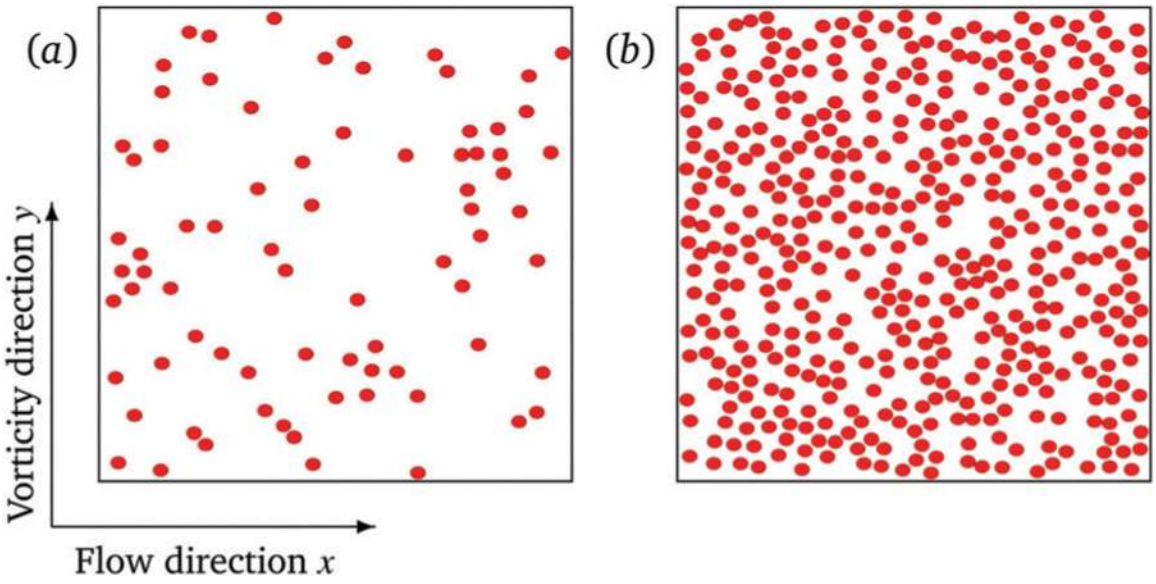

Fig. 8.

Initial conditions for the benchmark FD/FT simulations shown in Fig. 7 and for the QI and QI+STR calculations depicted in Fig. 9 and 10. Area fraction (a) $\phi_A = 0.05$ and (b) $\phi_A = 0.3$. The particles are randomly placed in the midplane of the channel. Flow and vorticity directions as indicated.

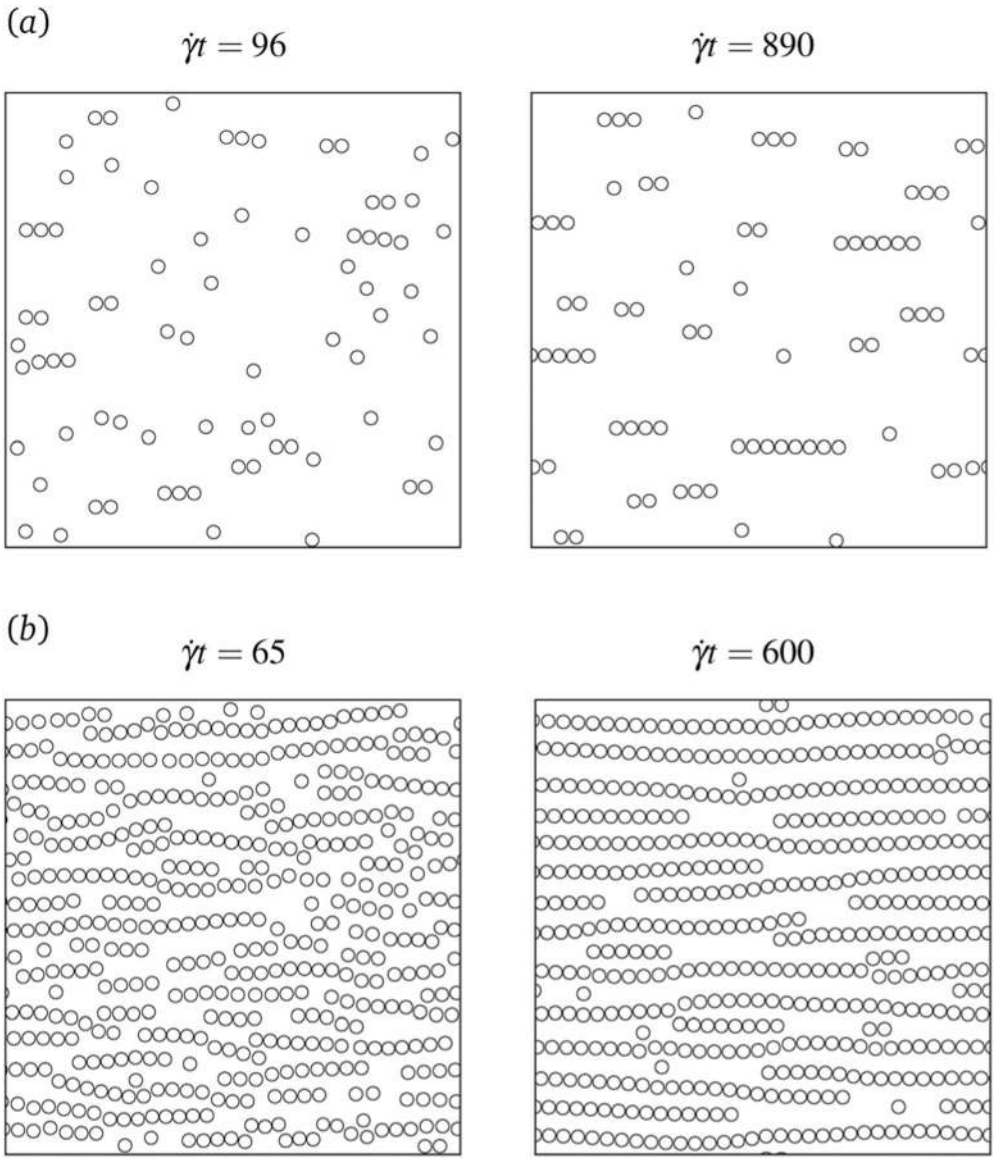

Fig. 9.

Predictions of the auxiliary QI model for the benchmark system. The evolution of the drop monolayer is shown for the area fraction (a) $\phi_A = 0.05$ and (b) $\phi_A = 0.3$. The drops form flow-oriented chains, but the microstructure of the monolayer (especially drop spacing) significantly differs from the benchmark FD/FT simulation results depicted in Fig. 7. The results demonstrate that the model is incomplete.

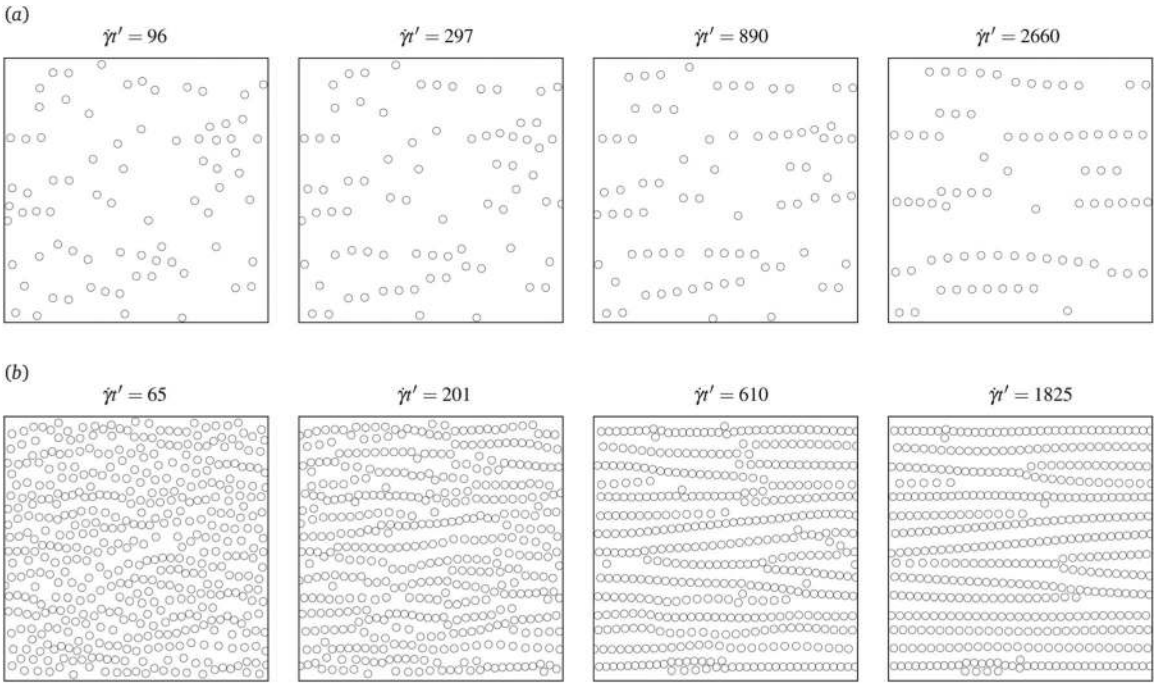

Fig. 10.

Predictions of the QI+STR model for the benchmark system. The evolution of the drop monolayer is shown for the area fraction (a) $\phi_A = 0.05$ and (b) $\phi_A = 0.3$ (also see ESI,† Movies M3 and M4). Drop configurations are labeled by the adjusted time $t' = t/\varepsilon$ with $\varepsilon =$ 0.6 for $\phi_A = 0.05$ and $\varepsilon = 0.2$ for $\phi_A = 0.3$. The time-adjusted results agree quantitatively for $\phi_A = 0.05$ and semi-quantitatively for $\phi_A = 0.3$ with the benchmark FD/FT simulations depicted in Fig. 7.

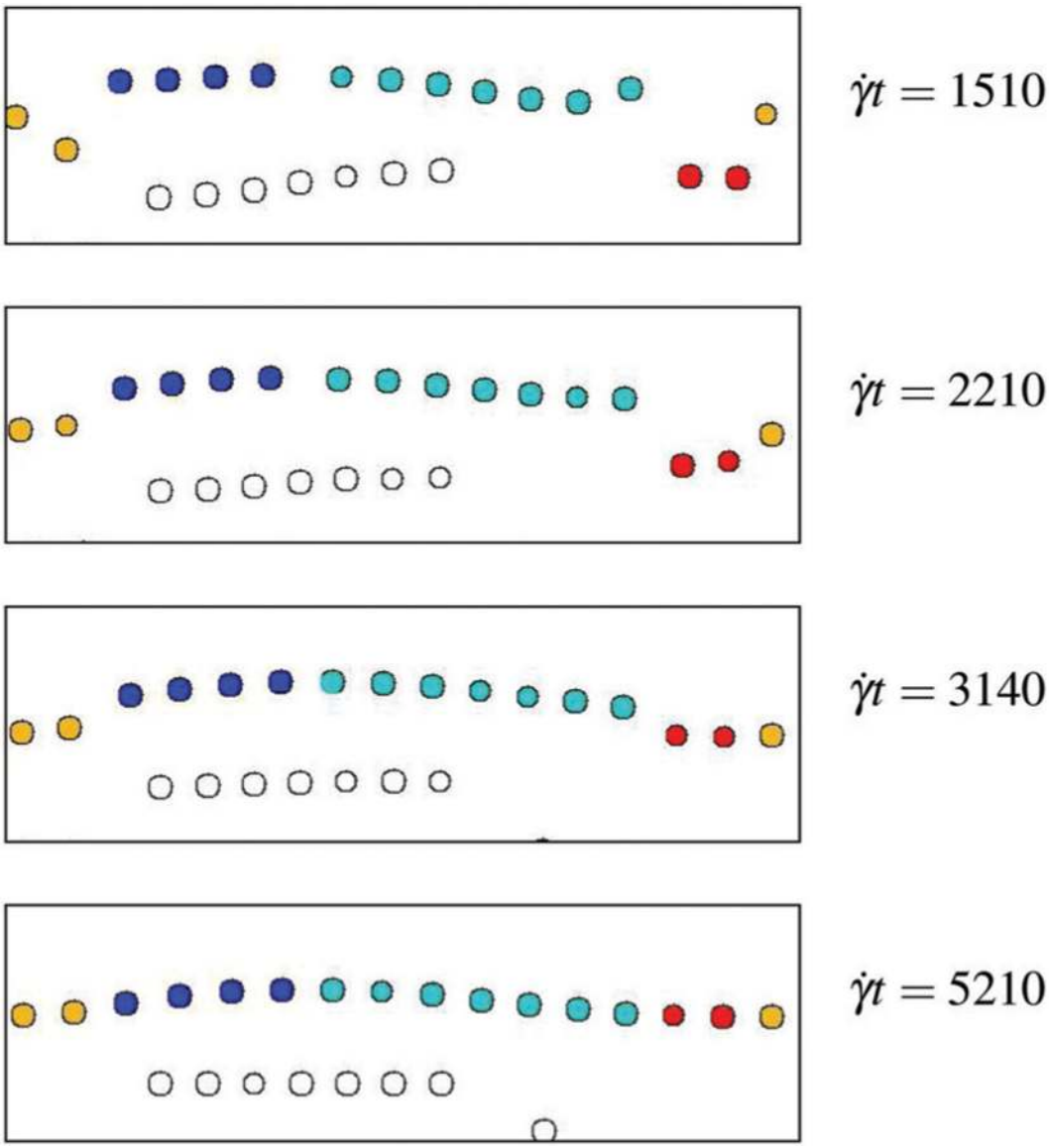

Fig. 11.

Chain merging by end-to-end connection. Initially disconnected short chains merging into a percolating chain are shown in different colors. The chains maintain approximately equal drop spacing throughout the process. (Results from QI+STR model).

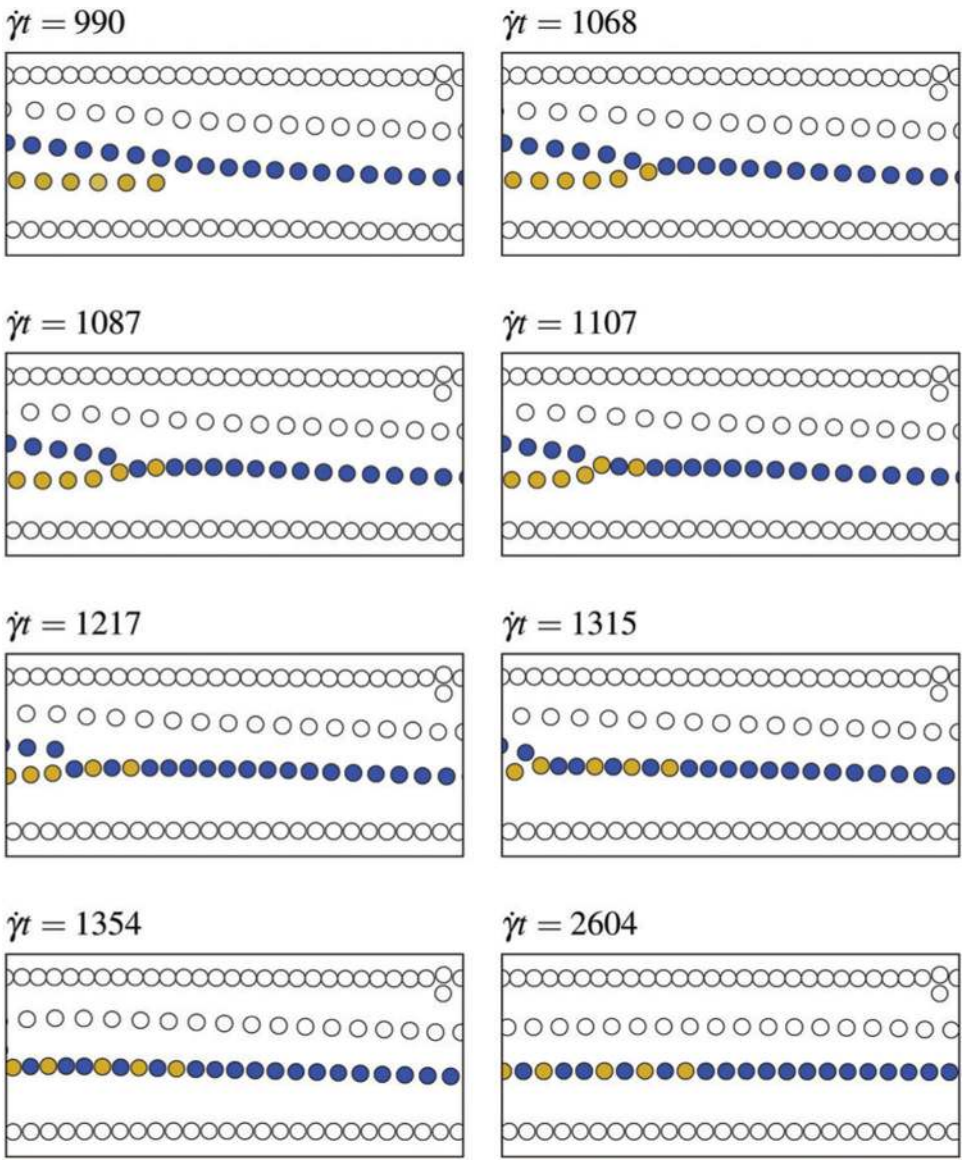

Fig. 12.

Chain merging by zipping. Two sparsely populated chains approach each other to form a y-shaped defect, and then merge in a chain zipping process in which particles are absorbed into a resulting denser chain. Drop spacing in the resulting chain is initially non-uniform, with tighter spacing in the zipping region. The spacing nonuniformities relax at long times; the relaxation is diffusive. (Results from QI+STR model).

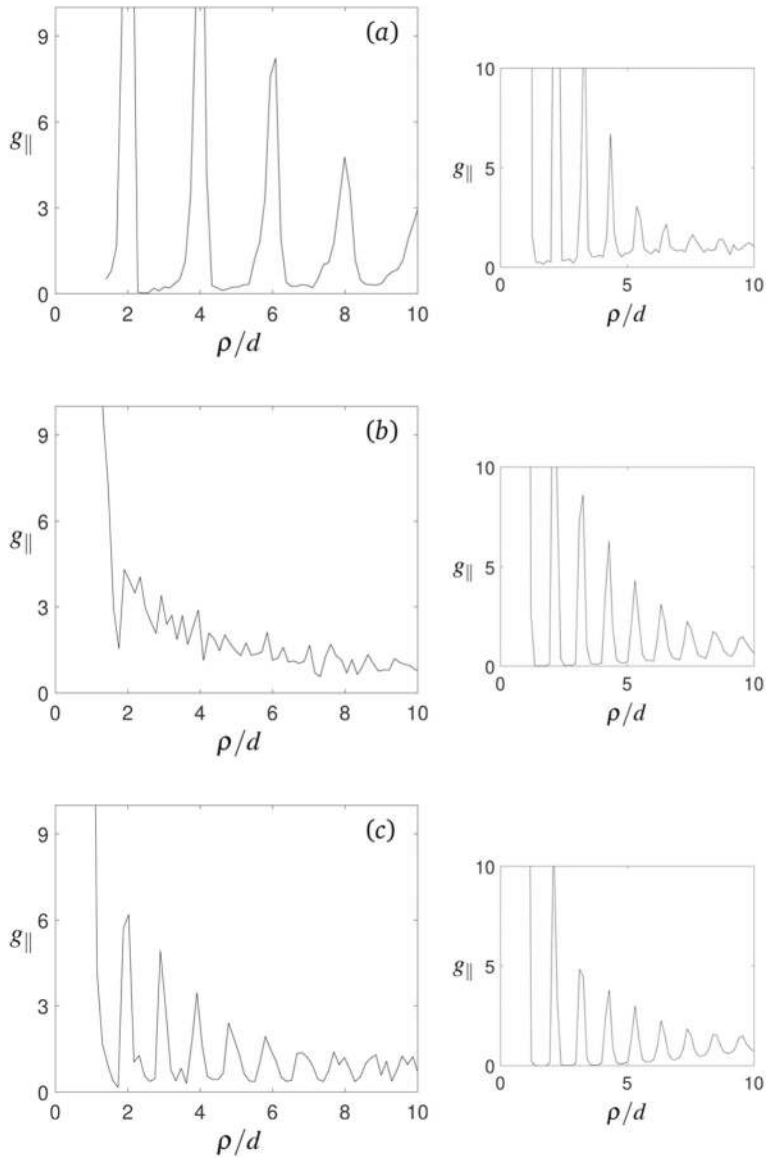

Fig. 13.

Long-time longitudinal pair correlation functions $g_\parallel$. Left panels show the results for the comprehensive QI+STR model and right panels provide the corresponding results for the auxiliary QI model for the area fraction (a) $\phi_A = 0.05$; (b) $\phi_A = 0.15$; and (c) $\phi_A = 0.3$ at time $\dot{\gamma}t = 4500$. According to the QI+STR model, at the area fraction $\phi_A = 0.05$ the pair correlation function $g_\parallel$ is sharply peaked, at $\phi_A = 0.15$ the peaks disappear, and they reemerge at $\phi_A = 0.3$. The graphs represent averages over 10 simulation runs for a system of 512 particles (see representative ESI,† Movies M5–M7).

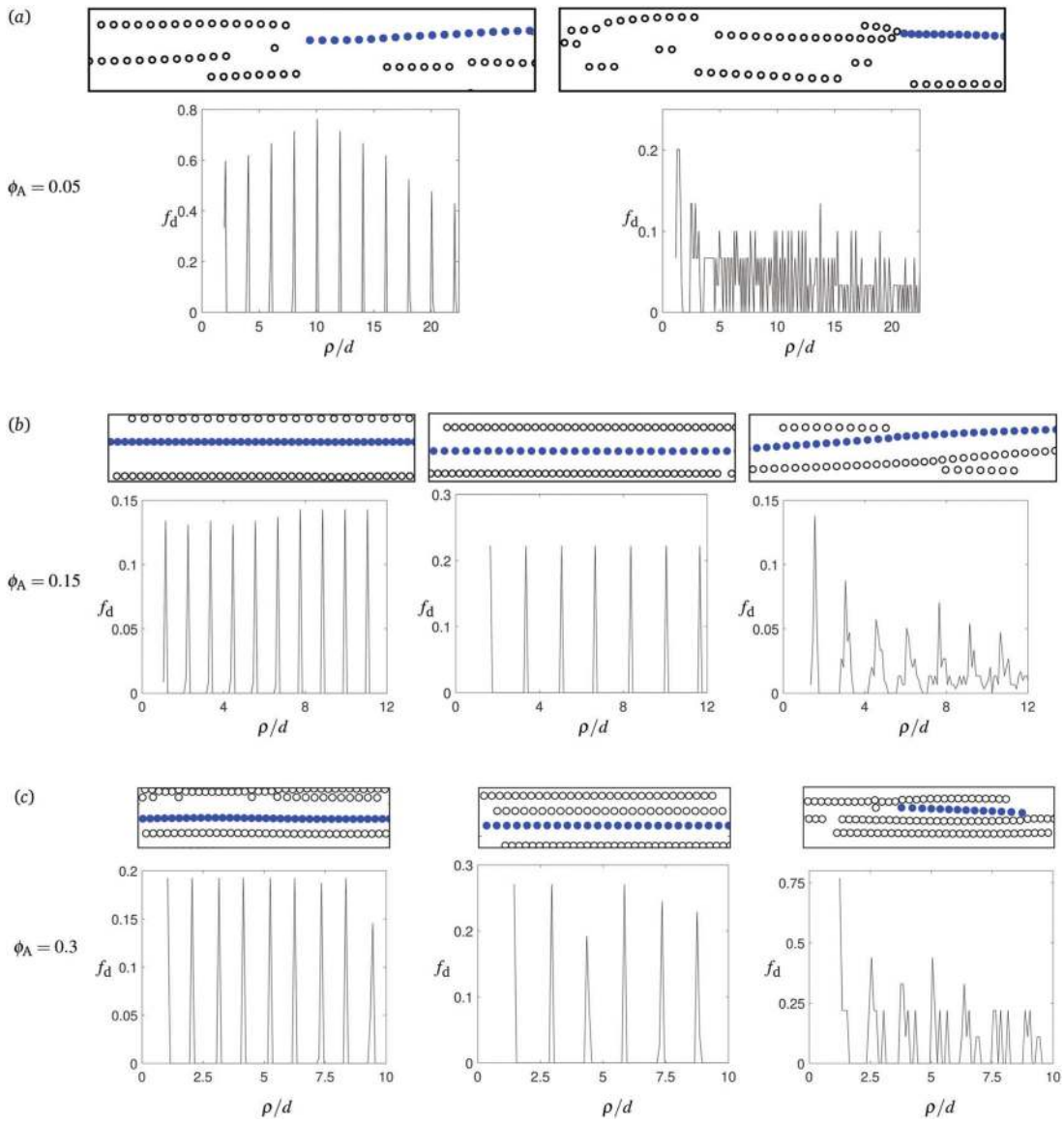

Fig. 14.

Representative examples of the probability distribution function of the drop-to-drop distance in selected drop chains in a QI+STR system at three area fractions (as labeled). The plots show the probability distribution f_d *vs.* the normalized drop separation ρ/d for the chains highlighted in blue in the simulation images shown above each plot. Samples are chosen to represent either equilibrated chains with small (left panels) and large (middle panels) spacing or unequilibrated chains with irregular spacing (right panels). Since the overall results indicate that for $\varnothing_A = 0.05$ most equilibrated chains have the same (large) spacing with drop separation $\rho \approx l_{st}$, no chain with a small spacing is shown. Examples of chains with irregular spacing (right panels) include (a) out-of-equilibrium chain undergoing zipping and (b and c) chains that are deformed because of hydrodynamic interactions with other chains. The results are presented for a system of 512 particles at time $\dot{\gamma}t = 4500$.

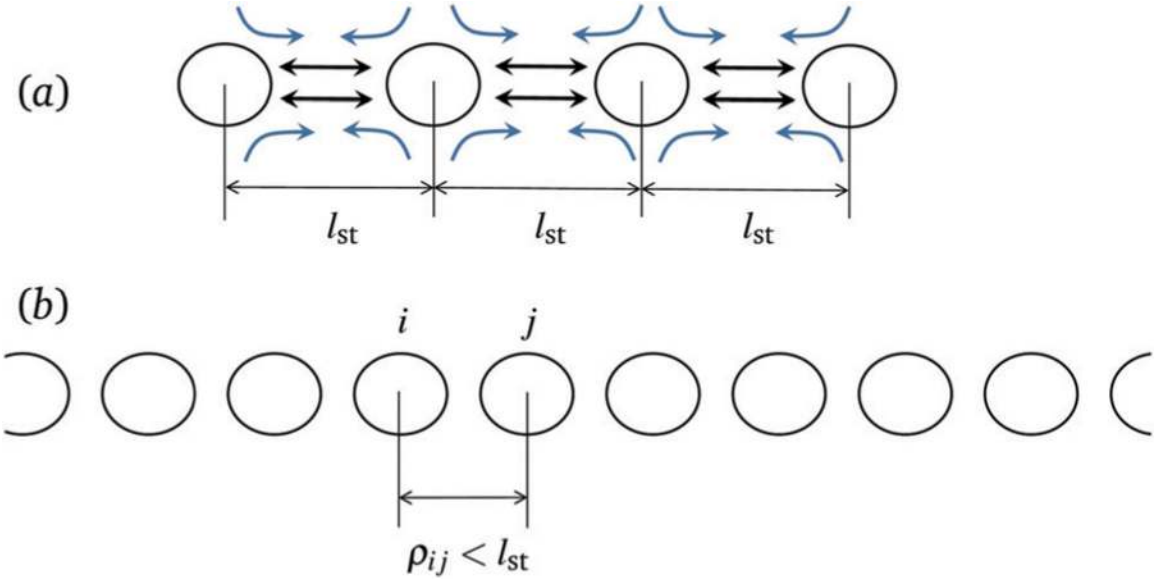

Fig. 15.

Definition of uncompressed and compressed chains. (a) An isolated finite chain relaxes to the uncompressed state with drop spacing l_{st}. Cyan arrows and black arrows represent the quadrupolar attraction and swapping-trajectory repulsion, respectively, which balance each other at drop separation l_{st}. (b) In a percolating compressed chain drop spacing is smaller than l_{st}. Since the swapping-trajectory repulsion is stronger than the quadrupolar attraction, the drops are subject to repulsive inter-drop hydrodynamic forces; the drops remain in equilibrium, however, because the repulsion from the left and right neighbors balances.

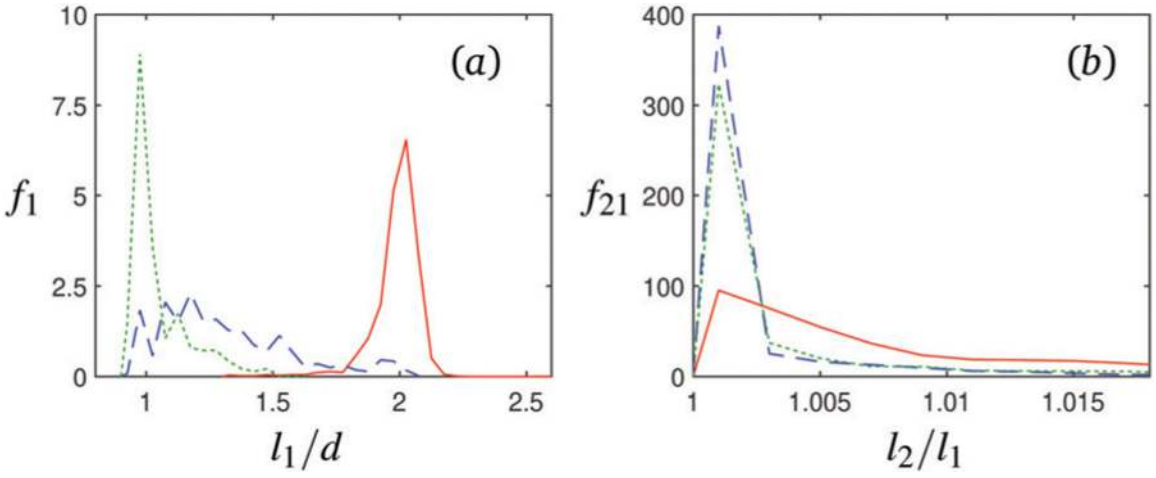

Fig. 16.

Statistics of the nearest-neighbor and second-nearest-neighbor distributions in the QI+STR system at long times. The probability distribution of (a) the normalized minimum drop-to-drop distance l_1/d and (b) the ratio l_2/l_1 of the second-to-first minimum distance for the area fraction $\phi_A = 0.05$ (red solid line), $\phi_A = 0.15$ (blue dashed), and $\phi_A = 0.3$ (green dotted) at time $\dot{\gamma}t = 4500$.

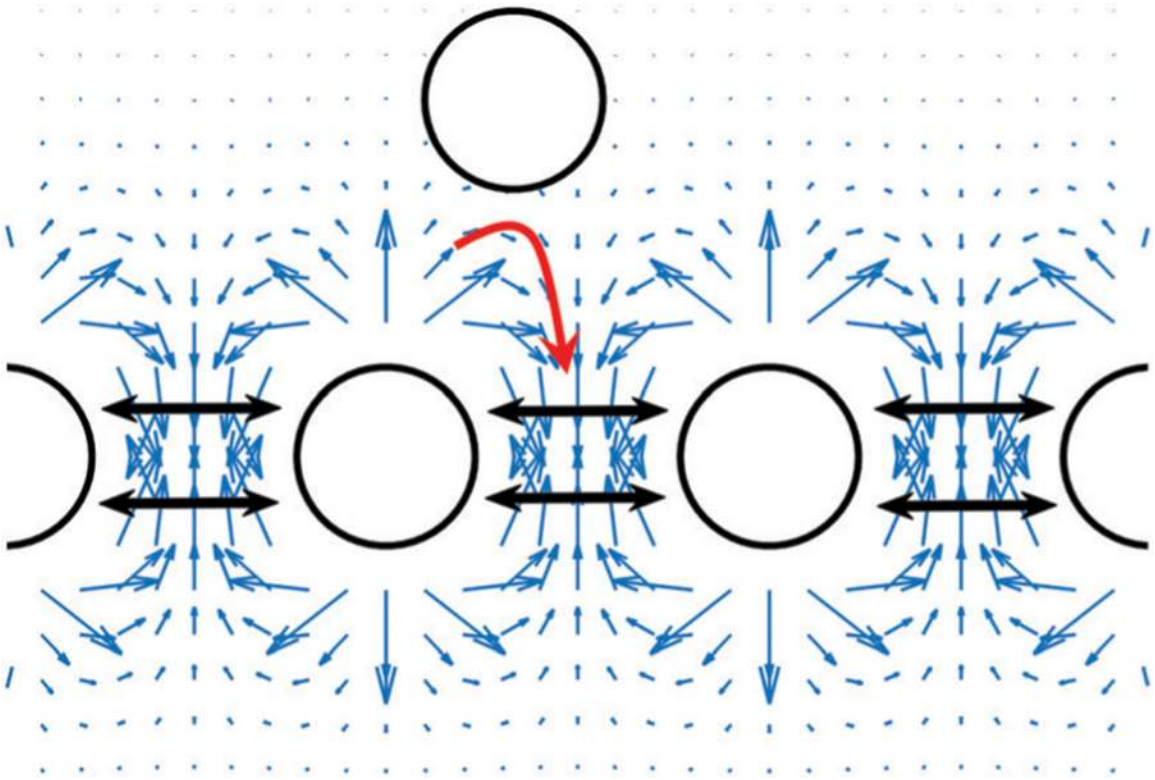

Fig. 17.

Incorporation of a new particle into a chain. The combined quadrupolar flow produced by the drops in the chain first positions the absorbed drop above a gap between chain particles and then pulls the particle into the chain. The swapping-trajectory repulsion acts only in the flow direction (along the chain); therefore, it maintains gaps between drops but does not hinder the absorption process.

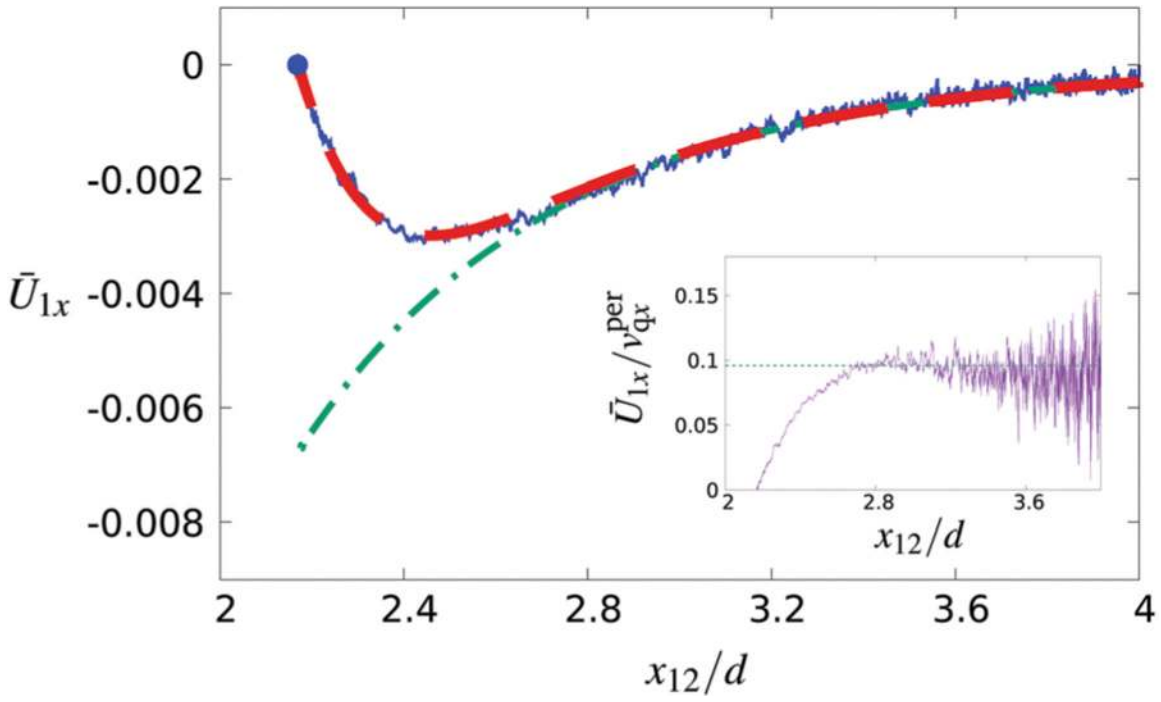

Fig. 18.

Matching the QI and QI+STR models to the two-particle benchmark FD/FT simulations in the intermediate- and far-field regimes. Main panel shows the normalized drop velocity $\bar{U}_{1x}$ *vs.* drop separation in a periodic system with a 23.04d × 3.84d unit cell and with drops initially aligned along the axis *x*. Benchmark simulations for drop velocity along the trajectory with initial drop separation $x_{12}/d = 4$ (solid blue line); quadrupolar interactions with matched quadrupolar moment (dot-dashed green line); quadrupolar interactions plus swapping trajectory repulsion with matched parameters listed in Table 1 (long-dashed red line). Blue circle indicates the stationary drop separation. The inset shows the ratio between the benchmark simulation data for $\bar{U}_{1x}$ and the periodic sum of the normalized quadrupolar velocity (9). The horizontal line in the inset represents the quadrupolar-moment value used in our models.

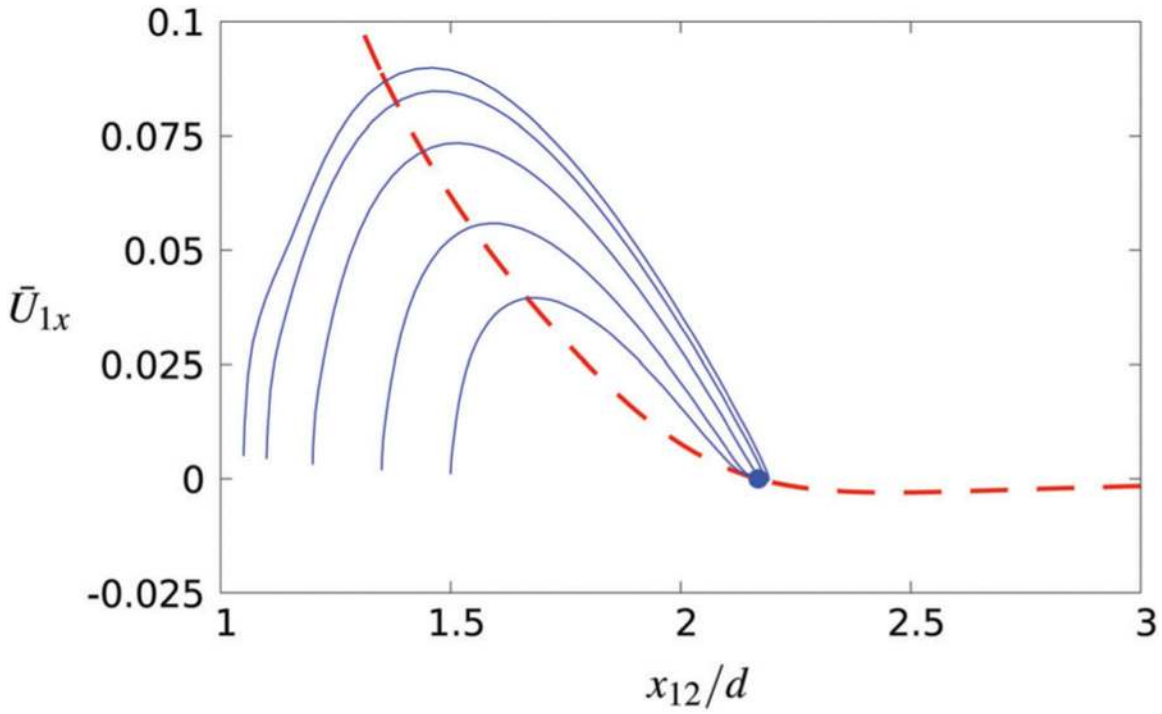

Fig. 19.

Matching the QI+STR model to the two-particle benchmark FD/FT simulations in the near-field regime. The figure shows the normalized drop velocity $\bar{U}_{1x}$ *vs.* drop separation in a system described in the caption of Fig. 18. Benchmark simulation results for the drop velocity along trajectories with initial drop separation $x_{12}^{(0)}/d = 1.05$, 1.1, 1.2, 1.35, and 1.5 (solid blue lines). Blue circle indicates the stationary drop separation. Quasistatic QI+STR result that qualitatively matches the FD/FT simulations (dashed red line); the parameters of the QI+STR model are listed in Table 1.

Table 1

Parameters of the QI and QI+STR models for the benchmark system

Quadrupolar moment	**Swapping-trajectory repulsion**			
Q	κd	b/d	ρ_o/d	B
0.096	5.8	0.5	1.90	2.32